# Simulation of calcium signaling in fine astrocytic processes: Effect of spatial properties on spontaneous activity

Audrey Denizot[1,2], **Misa Arizono**[3,4], **U. Valentin Nägerl**[3,4], **Hédi Soula**[1,5], **Hugues Berry**[1,2]*

1 INRIA, F-69603, Villeurbanne, France, **2** Univ Lyon, LIRIS, UMR5205 CNRS, F-69621, Villeurbanne, France, **3** Interdisciplinary Institute for Neuroscience, Université de Bordeaux, Bordeaux, France, **4** Interdisciplinary Institute for Neuroscience, CNRS UMR 5297, Bordeaux, France, **5** Univ P&M Curie, CRC, INSERM UMRS 1138, F-75006, Paris, France

* hugues.berry@inria.fr
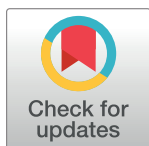
Abstract

Astrocytes, a glial cell type of the central nervous system, have emerged as detectors and regulators of neuronal information processing. Astrocyte excitability resides in transient variations of free cytosolic calcium concentration over a range of temporal and spatial scales, from sub-microdomains to waves propagating throughout the cell. Despite extensive experimental approaches, it is not clear how these signals are transmitted to and integrated within an astrocyte. The localization of the main molecular actors and the geometry of the system, including the spatial organization of calcium channels IP_3R, are deemed essential. However, as most calcium signals occur in astrocytic ramifications that are too fine to be resolved by conventional light microscopy, most of those spatial data are unknown and computational modeling remains the only methodology to study this issue. Here, we propose an IP_3R-mediated calcium signaling model for dynamics in such small sub-cellular volumes. To account for the expected stochasticity and low copy numbers, our model is both spatially explicit and particle-based. Extensive simulations show that spontaneous calcium signals arise in the model via the interplay between excitability and stochasticity. The model reproduces the main forms of calcium signals and indicates that their frequency crucially depends on the spatial organization of the IP_3R channels. Importantly, we show that two processes expressing exactly the same calcium channels can display different types of calcium signals depending on the spatial organization of the channels. Our model with realistic process volume and calcium concentrations successfully reproduces spontaneous calcium signals that we measured in calcium micro-domains with confocal microscopy and predicts that local variations of calcium indicators might contribute to the diversity of calcium signals observed in astrocytes. To our knowledge, this model is the first model suited to investigate calcium dynamics in fine astrocytic processes and to propose plausible mechanisms responsible for their variability.

Author summary

Astrocytes process information in the brain via calcium signals that can modulate neuronal communication. Astrocytic calcium signals are associated with brain functioning, including memory and learning, and are altered in the diseased brain. Astrocytic calcium signals display a huge spatio-temporal diversity, which mechanisms and functional roles are poorly understood. 80% of calcium signals occur in the gliapil, corresponding to astrocytic ramifications that are too thin to be detected by conventional light microscopy. Because of the small volumes at stake, we modeled astrocytic calcium signals in the gliapil with a stochastic spatially-explicit individual-based model. Our model successfully reproduces calcium signals that we measured in hippocampal astrocytic gliapil and sheds light to the importance of the localization of calcium sources. We predict that the diversity of calcium signals measured with fluorescent indicators might be partly due to local variations of the concentration of those indicators. We believe that this model will be useful to investigate the propagation of calcium signals within the sponge-like network of astrocytic processes, and eventually to better understand information processing in the brain.

Introduction

Astrocytes were first characterized as non-excitable cells of the central nervous system since, although they express voltage-gated channels [1], they do not exhibit electrical excitability [2]. Astrocytes excitability instead results from variations of cytosolic calcium concentration [3]. At the cellular level, those calcium signals emerge in astrocytes in response to synaptic activity and may cause the release of molecules called gliotransmitters such as glutamate, ATP, tumor necrosis factor-α, or D-serine, which can modulate synaptic transmission [4–7] and vasoconstriction/vasodilatation [8–11]. This close association of astrocytes to pre- and post- synaptic elements, both structurally and functionally, is referred to as tripartite synapse (see e.g. [12–15] for reviews on tripartite synapses and the associated controversies). On a larger scale, astrocytic calcium signals can modulate neuronal synchronization and firing pattern [16–18] and have been observed *in vivo* in response to external stimuli [19, 20]. Altogether, those observations disrupt the traditional view that allocates information processing in the brain to neurons only.

Cell culture, *ex vivo* and *in vivo* studies have demonstrated that astrocytes display both spontaneous calcium signals [19, 21–25] and neuronal activity-induced calcium signals [17, 20, 26]. Astrocytic calcium signals can be localized to synapses [4, 26–28], propagate along processes [29], lead to whole-cell events [30] or even propagate to other cells [31]. Whether this spatio-temporal variability of calcium signals is associated to different physiological functions and whether this could reflect signal integration from different neural circuits is still unknown.

Astrocytic calcium signals are considered to rely mainly on the IP_3R calcium channel pathway. Indeed, type-2 IP_3R calcium channel is enriched in astrocytes [32] and knocking-out IP_3R2 channels abolishes all calcium signals in astrocytic soma and roughly half of them in the cell processes [28]. The molecular origin of the IP_3R2-independent signals in processes remains a matter of debate, and could involve calcium fluxes through the plasma membrane [28] and/or other IP_3R channel subtypes [33]. In any case, astrocytes respond to G-protein-coupled receptor (GPCR) agonists with calcium transients [34, 35]. Binding of agonists to $G_{q/11}$-GPCRs activates IP_3 synthesis. In turn, binding of both IP_3 and calcium ions to IP_3R channels on the membrane of the endoplasmic reticulum (ER) triggers a calcium influx from the ER to the cytosol [36]. The initiation and propagation of calcium signals within astrocytes

then relies on the so-called calcium-induced-calcium release (CICR) mechanism: an increase, even small, of the local calcium concentration increases IP_3R opening probability thus increasing the probability for local calcium concentration to rise further.

80% of the astrocyte calcium activity *in vivo* take place in the gliapil, which is mostly formed by astrocytic ramifications that cannot be spatially resolved by conventional light microscopy [37], yet account for 75% of the astrocytic volume [38]. According to electron microscopy studies, the perisynaptic astrocyte projections (PAPs) that belong to the gliapil could be as thin as 30-50nm in diameter [39, 40]. At this spatial scale, calcium signals are characterized by non-uniform spatial distributions composed of hotspots where calcium signals are more likely to occur and repeat [41, 42]. Those observations suggest the existence of subcellular spatial organizations responsible for the spatial distribution of calcium signal patterns. Understanding calcium signaling in PAPs, where astrocytes potentially regulate neuronal information processing, is crucial. However, only calcium signals in thicker processes, around 300nm in diameter, are within reach of current conventional imaging methods [40] and most studies on astrocytic calcium have focused on astrocytic soma and main processes, where characteristics and physiological roles of calcium signals are likely to differ from those of PAPs. Because of the small dimensions and volumes at stake, modeling is currently the only approach that can investigate calcium signal generation, transmission and the effect of spatial properties within PAPs.

Mathematical models of CICR-based signaling date back to the beginning of the 1990s (for recent reviews see e.g. [43–45]). The first IP_3R-mediated calcium signaling models assumed perfect mixing of the molecular species and deterministic kinetics (ordinary differential equations) and typically treated IP_3 concentration as a parameter [46–48]. In those models, calcium transients emerge as limit-cycle oscillations from a Hopf bifurcation (or a saddle-node on an invariant circle) beyond a critical value of the IP_3 concentration. The first astrocyte-specific calcium signaling models arose a decade later. In those models, the IP_3 concentration is usually a dynamical variable coupled to calcium but calcium transients still emerge through the Hopf-bifurcation scenario. Notably, those models focused on intercellular IP_3 transport within astrocyte networks via gap junctions [49, 50]. Stochastic models of IP_3R-mediated calcium signaling have also been proposed, that take into account the stochasticity associated with molecular interactions [51–54]. Yet, none of those studies accounts both for molecular species diffusion and stochasticity of the reactions taking place inside astrocytes, which is essential for modeling the stochastic effects associated with small volumes and the low copy number of molecules or ions involved in fine processes. Recently, individual-based modeling has been introduced to evaluate the impact of diffusive noise on IP_3R opening dynamics [55], but this simplified model disregarded IP_3 dynamics and restricted stochasticity to the vicinity of the IP_3Rs.

Here, we propose an IP_3R-mediated calcium signaling model adapted to the dynamics of CICR in small spatial volumes corresponding to thin PAPs. To account for the stochasticity inherent to small sub-cellular volumes and low copy numbers expected in fine processes, our model is both spatially explicit and particle-based: each molecule is described individually, diffuses in space through a random walk and reacts stochastically upon collision with reaction partners. The kinetics of IP_3R channels is accounted for with a simplified version of the 8-state Markov model on which most of the previous CICR models are based. In order to explore the range of dynamical behaviors that the model can display, we first focus on a 2D version of our model, that is less compute-intensive than the 3D version. Extensive simulations of the 2D model show that spontaneous calcium signals arise in the model via the interplay between the excitability of the system and its stochasticity. The model accounts for various forms of calcium signals ("blips" and "puffs") and their frequency depends on the spatial organization of the IP_3R channels. In particular, we demonstrate that the co-localization of sources of calcium

influx plays a crucial role in triggering an effect of IP_3R clustering on calcium signaling. Finally, as solute concentrations can hardly be defined in 2D, we use a 3D version of the model in order to compare it to experimental data. We show that the spontaneous calcium signals generated by the 3D model with realistic process volume and astrocytic calcium concentrations successfully reproduce the spontaneous calcium transients measured in calcium microdomains with confocal microscopy in organotypic culture of hippocampal astrocytes. Our simulations predict that local variations of the concentration of calcium indicators such as GECIs might contribute to the diversity of calcium signals observed in astrocytes so that precise monitoring of their concentration should be performed. Our model therefore represents the first validated tool to investigate calcium signals in realistic small sub-cellular volumes such as in PAPs, where astrocytes and synapses communicate. This provides a crucial step towards a better understanding of the spatiotemporal response patterns of astrocytes to neuronal activity and beyond, towards astrocyte-neuron communication.

Results

Spontaneous oscillations in the model

We first analyzed our particle-based model for the CICR signaling system of Fig 1, with parameter values presented in Table 1. To that end, we compared Monte-Carlo simulations of the particle-based model in two dimensions with the corresponding Mean-Field and Gillespie's SSA models (see Methods section). Those three models represent different levels of approximation: the Mean-Field model assumes deterministic kinetics and perfect mixing; the SSA model keeps the perfect mixing hypothesis but assumes stochastic kinetics while the particle-based model assumes stochastic kinetics but accounts for potential non-perfect mixing, i.e. diffusion effects. For comparison with SSA, we first considered perfect mixing of Ca^{2+} ions and IP_3 molecules in the particle-based model by setting the diffusion coefficients $D_{Ca} = D_{IP3} = \infty$ (see Method section).

Fig 2A shows one simulation sample for each model. A first result is that the stochastic models (SSA and particle-based) do exhibit spontaneous calcium peaks with the parameters of this figure. On top of a background level of approximately 50 Ca^{2+} ions, with fluctuations of roughly ± 20 ions, large and fast peaks arise spontaneously with a total amplitude between 20 and 120 ions above the baseline. In strong opposition, the (deterministic) mean-field model does not show these oscillations: one gets a stationary trace, that systematically coincides with the baseline level of the stochastic traces (Fig 2B). Comparing the two stochastic models (SSA and particle-based) indicates that both display the same basal calcium level (Fig 2B) and the same frequency and mean peak amplitude (Fig 2C). Altogether, this suggests that stochasticity is necessary for spontaneous calcium signals to occur in this model.

We next searched for the dynamical mechanism that gives rise to those spontaneous peaks. A thorough numerical parameter exploration of the mean-field model failed to demonstrate the existence of Hopf bifurcations or of any other bifurcation that would generate limit-cycle oscillations in the model. This is a distinctive feature of our model, since spontaneous oscillations in the vast majority of IP_3R-mediated calcium signaling models arise from limit-cycle generating bifurcations [46–48]. This is however not unexpected since the simplifications made to derive our model significantly reduced its nonlinearity compared to these models, and the emergence of limit-cycle bifurcations demands strong nonlinearity. For instance, limit-cycle oscillations in the classical Li and Rinzel model [48] disappear when IP_3R opening needs less than three open monomers. However, our model retains enough nonlinearity to exhibit excitability. To demonstrate this, we used the mean-field model, waited until all concentrations reached their stationary state, and injected an increasing amount of exogenous IP_3

A Kinetic scheme

B IP3R model

C Spatial organization
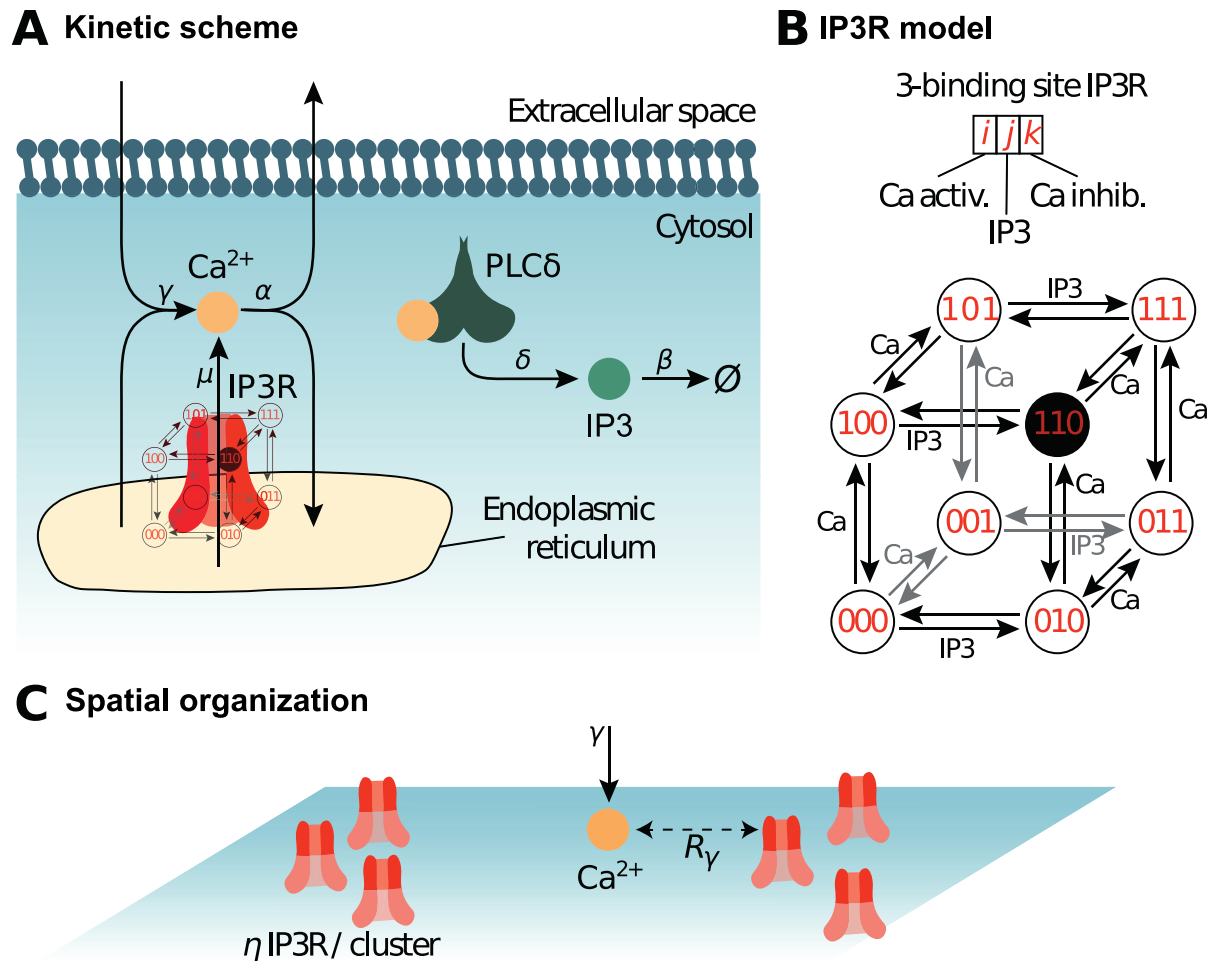
Fig 1. Reaction scheme and IP_3R model. The biochemical processes included in the model are illustrated in (A). Cytosolic calcium can exit the cytosol to the extracellular space or the endoplasmic reticulum (ER) at a (total) rate α, lumping together the effects of ER and plasma membrane pumps. Likewise, Ca^{2+} can enter the cytosol from the extracellular space or from the ER via IP_3R-independent flow, with (total) rate γ, emulating calcium channels from the plasma membrane. When an IP_3R channel opens, calcium enters the cytosol through the channel at rate μ. Phospholipase Cδ (PLCδ), once activated by calcium binding, produces IP_3 at rate δ. Like Ca^{2+}, IP_3 can bind the IP_3R channel and is removed with rate β. (B) Our model of the kinetics of the IP_3R channel is an 8-state Markov model adapted from [46, 56]. Each IP_3R channel monomer is associated with 3 binding sites, two calcium binding sites and one IP_3 binding site. Occupancy states are designated by a triplet {i, j, k} where i stands for the occupation of the first Ca binding site (i = 1 if bound, 0 else), j for that of the IP_3 binding site and k for the second Ca site. The first calcium binding site has higher affinity than the second. The open state is state {110}, where the first Ca and the IP_3 sites are bound but not the second Ca site. (C) Spatial parameters for the particle-based model. The N_{IP_3R} IP_3R molecules are positioned within uniformly distributed clusters, with η IP_3R in each cluster. Hence $\eta = 1$ corresponds to uniformly distributed IP_3R (no clustering), while the degree of clustering increases with η (for constant total IP_3R number). To account for potential co-localization between IP_3R-dependent and IP_3R-independent calcium sources, the influx of IP_3R-independent calcium (at rate γ) occurs within distance R_γ of an IP_3R. Thus, low values of R_γ emulate co-localization between IP_3R-dependent and IP_3R-independent Ca^{2+} influx sources.

https://doi.org/10.1371/journal.pcbi.1006795.g001

molecules. In response to this IP_3 injection, a calcium transient was obtained, before relaxation to the stationary state (Fig 2D). Fig 2D2 shows how the resulting transient amplitude depends on the amount of injected IP_3. For low values of IP_3R calcium binding rate (first site), a_1, the calcium response is basically linear with the number of injected IP_3: doubling the amount of IP_3 injected only doubles the amplitude of the calcium response. However, as a_1 increases, peak amplitude becomes a strongly nonlinear function of the number of IP_3 injected. With $a_1 = 5$ a.u. for instance, doubling the number of injected IP_3 from 50 to 100 results in an almost threefold increase of the calcium response. Therefore the mean-field model with large values

Table 1. Parameter values and initial conditions of the 2D model. a.u: arbitrary unit. In 2d, by definition, a MC time unit is 100 Δt and one MC space unit is set by the interaction radius of IP_3R, i.e. $d_{IP_3R} = 1.0$ MC space unit. $\delta, \beta, \mu, \gamma, b_1, b_2$ and b_3 are first order constants, in (MC time unit)$^{-1}$. Diffusion coefficients D_{Ca} and D_{IP3} are expressed in (MC space unit)^2.(MC time unit)$^{-1}$ whereas α, a_1, a_2, a_3 are expressed in (MC space unit)^2.(MC time unit)$^{-1}$.

Parameter	Description	Value in 2d model
V	Cell volume	200×200 a.u.
	IP$_3$ dynamics	
IP_0	Initial IP_3 number/conc.	15 molec.
D_{IP3}	IP_3 diffusion	10 a.u
N_{plc}	PLCδ number/conc.	1000 molec.
δ	PLCδ max rate	0.1 a.u
β	IP_3 decay	0.01 a.u
	Ca^{2+} dynamics	
Ca_0	Initial Ca^{2+} number/conc.	50 molec.
D_{Ca}	Ca^{2+} diffusion	varied
μ	Ca^{2+} flux through open IP_3R	50 a.u
γ	cytosolic Ca^{2+} influx	50 a.u
α	Ca^{2+} decay rate	1.0 a.u
	IP$_3$R	
N_{IP_3R}	IP_3R number	1000 molec.
d_{IP_3R}	IP_3R interact. distance	1 space unit
	IP$_3$R binding	
a_1	First Ca	1.0 a.u
a_2	IP_3	1.0 a.u
a_3	Second Ca	0.1 a.u
	IP$_3$R dissociation	
b_1	First Ca	0.1 a.u
b_2	IP_3	0.1 a.u
b_3	Second Ca	0.1 a.u

https://doi.org/10.1371/journal.pcbi.1006795.t001

of a_1 is an excitable system that amplifies the fluctuations of IP_3 in its calcium responses. We conclude that spontaneous calcium transients occur in the system of Fig 1 through the interplay of the stochasticity of the SSA or particle-based models and the underlying excitability of the system.

Transitions between calcium activity regimes

The experimental and modeling literature on intracellular calcium signals distinguishes two classes of localized calcium peaks: puffs and blips [57]. Blips refer to brief and weak peaks that correspond to the opening of a single IP_3R channel (or a single IP_3R channel tetramer), whereas puffs are longer and higher peaks resulting from the concerted opening of a group of nearby IP_3R channels (or tetramers thereof), via the calcium-induced calcium-release principle. We next examined whether our model was able to reproduce these observations.

We carried out parameter exploration of the particle-based model in conditions of perfect mixing for mobile molecules (*Ca* and *IP$_3$*) and uniform spatial distribution of the immobile ones (PLCδ, *IP$_3$R*). As expected, we found that calcium peaks frequency depends on parameter values (Fig 3A). When the rate of calcium influx through open IP_3R channels μ or the binding rate constant to the first Ca IP_3R site a_1 are too small, the model does not exhibit calcium peaks at all, only fluctuations around a stationary state (Fig 3C★). This is in agreement with
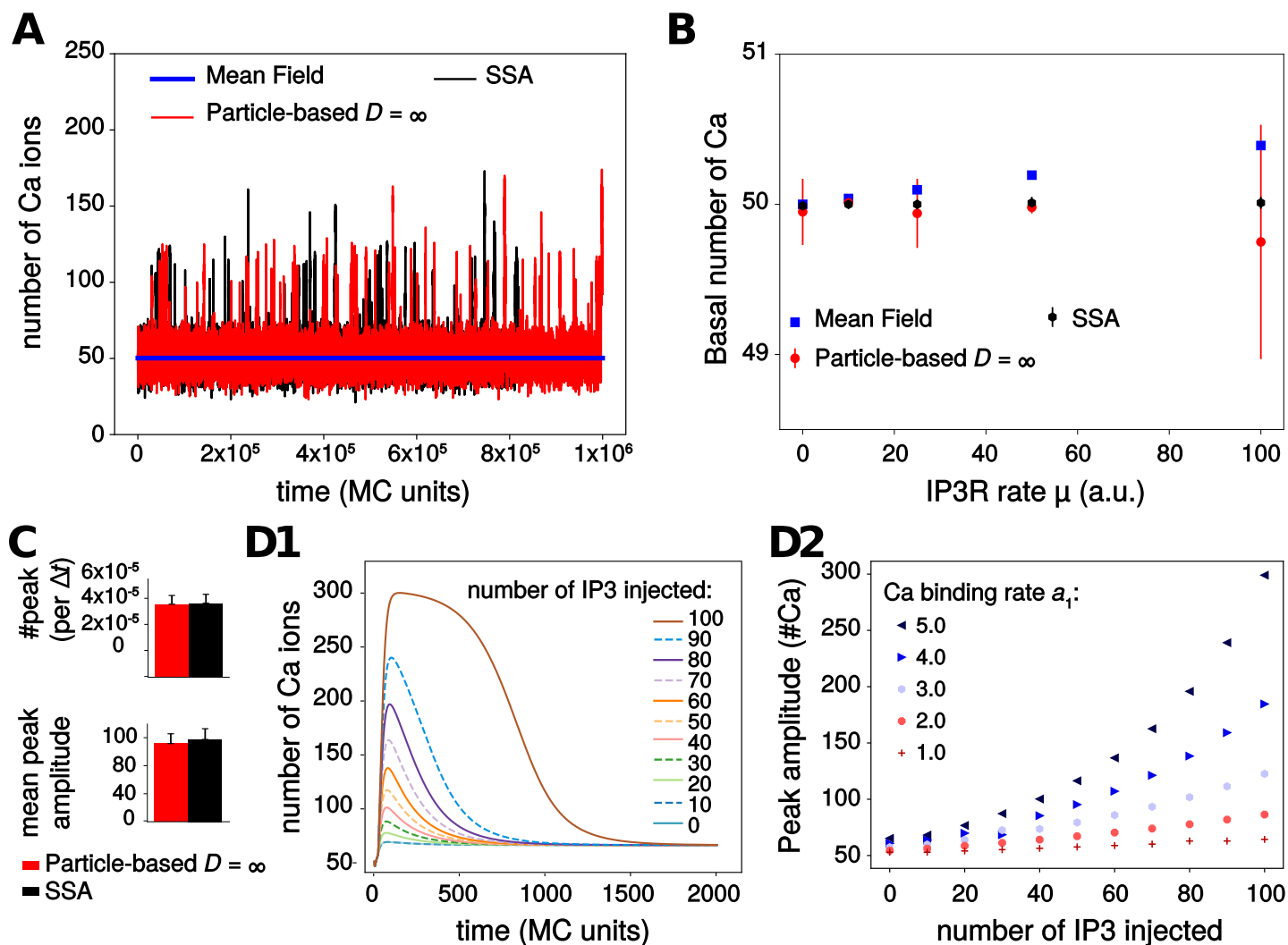
Fig 2. Model exploration. (*A*) Spontaneous transients are observed in simulations of the particle-based and the Gillespie's SSA model but not in the Mean Field model. (*B*) The three models display the same basal calcium level when μ, the calcium influx rate through open IP_3R channels, increases. The higher variability in the stochastic models reflects the integer value of basal calcium (either 49 or 50, depending on simulations). (*C*) Quantification of calcium transients in the stochastic models (calcium peak frequency and mean peak amplitude). No significant difference between the two models was observed. (*D*) Excitability of the Mean-Field model: increasing quantities of exogenous IP_3 molecules were injected at time $t = 20\Delta t$, after model equilibration. The amplitude of the resulting calcium response (*D1*) was quantified depending on the amount of IP_3 injected and the value of the binding rate constant to the first calcium IP_3R site, a_1 (*D2*). Parameter values for the particle-based model: $D_{Ca} = D_{IP3} = \infty$ (perfect mixing) and $\eta = 1$, $R_\gamma = 200$, i.e. no IP_3R channels clustering, and no co-localization of IP_3R with IP_3R-independent Ca^{2+} sources. For SSA and particle-based models, the figure shows the average ± standard deviation over 20 simulations.

our analysis of the system excitability above, that evidenced excitability only for large enough values of a_1 (Fig 2D2). Note however that in the model, IP_3R openings do not necessarily lead to a calcium peak, especially for low values of both μ and a_1 (Fig 3C★). Spontaneous calcium transients are obtained in the particle-based model beyond threshold of (μ, a_1) values, with a peak frequency that increases with parameters values (Fig 3A). Inspection of the maximal number of open IP_3R per peak reveals that not only the frequency, but also the type of these transient signals changes with parameters values (Fig 3A): the less frequent signals are generally associated with a single open IP_3R per peak (Fig 3C■), corresponding to blips, whereas the high-frequency spontaneous signals rely on the opening of $2 - 12$ IP_3R in a peak (Fig 3C●), corresponding to puffs. In agreement with experimental observations [58, 59], calcium
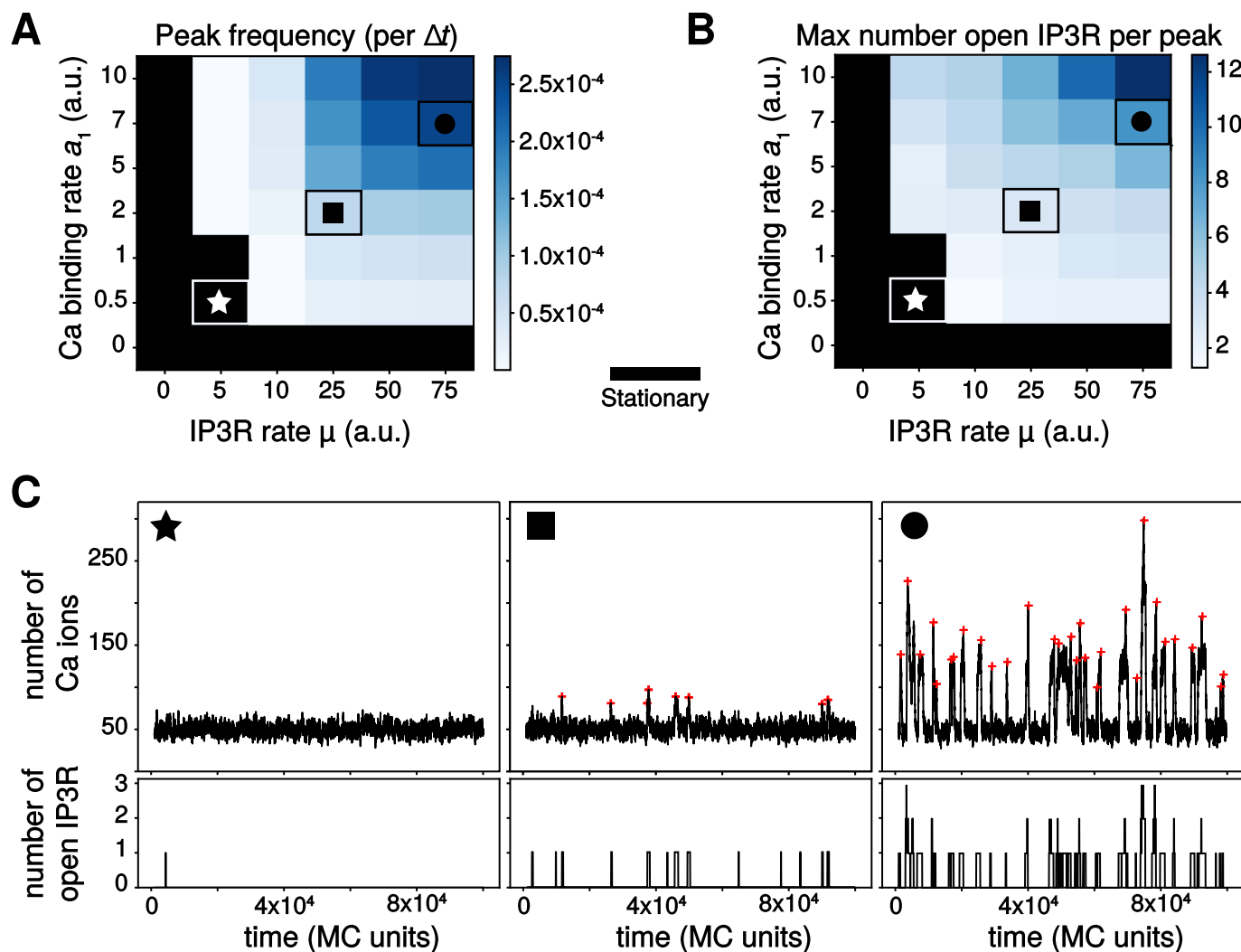
Fig 3. The particle-based model produces different calcium activity regimes depending on parameter values. Color-coded map of variation of the peak frequency, expressed as the number of calcium peaks per MC time step (*A*) and as the maximal number of IP_3R channel open per peak (*B*). The color scale is given for each map. The black area corresponds to the stationary regime. Note that the *x* and *y*-axis scales in (*A*) and (*B*) are not regularly spaced. The symbols ★, ■ and ● locate parameter pairs that are illustrative of the three dynamical regimes shown in (*C*): stationary (★, $\mu = 5$, $a_1 = 0.5$), blips (■, $\mu = 25$, $a_1 = 2$) and puffs (●, $\mu = 75$, $a_1 = 7$). Red crosses show the locations of peaks from automatic detection. $D_{Ca} = D_{IP3} = \infty$, $\eta = 1$, $R_\gamma = 200$.

https://doi.org/10.1371/journal.pcbi.1006795.g003

puffs in the particle-based model are characterized by higher peak amplitude and peak duration compared to blips. Taken together, these results show that our particle-based model not only reproduces the existence of spontaneous calcium peaks in conditions of low copy numbers, it is also able to reproduce the existence of different types of localized calcium transients, in agreement with experimental measurements.

Impact of calcium diffusion coefficient on calcium signals

A modeling study has demonstrated the necessity to account for the stochasticity inherent to calcium diffusion when modeling calcium signaling in small volumes [60]. We next investigated the impact of calcium diffusion on calcium dynamics in the particle-based model. In neurons or astrocytes, the amount of endogenous calcium buffers is large so that the diffusion distance of free calcium is believed to be very small. Many of the endogenous buffers are

however mobile. Buffers can have a very significant effect on calcium dynamics because they decrease the diffusion distance and the effective diffusion coefficient of calcium ions [53, 54, 61–64]. Here, we have chosen not to include buffers explicitly in the model for the sake of model simplicity, but to account for their presence by decreasing the diffusion coefficient for calcium. Therefore, the latter is to be interpreted as an effective diffusion coefficient lumping together calcium buffering by mobile endogenous buffer and diffusion of these buffers. To confirm that explicit addition of buffers yields effects similar to a decrease of the Ca^{2+} diffusion coefficient, we have explicitly added endogenous buffer molecules to our 2D model in a subset of simulations, assigning a low coefficient of diffusion for buffers and high one for free calcium ions. These simulations confirmed the absence of significant difference between simulations obtained using fast calcium diffusion and slow explicit buffers on the one hand, and our reference model without buffers but with an effective lower D_{Ca} on the other hand (S1 Fig).

Moreover, several plasma membrane proteins, in particular the Na^+-Ca^{2+} exchanger (NCX) have been observed to co-localize with ER proteins in neurons and astrocytes [65]. Such a co-localization of calcium signaling molecules might imply spatial organizations including raft-like micro-domains. This organization seems essential for calcium wave propagation in astrocytes [66]. Moreover, mGluR5-ER proteins co-clusters mediated by an interaction with Homer1 scaffold protein have been observed in astrocytic processes [67]. Homer1 is also known for increasing calcium activity in neurons by increasing IP_3R-mGluR5 proximity [68]. Those experimental studies suggest that several calcium sources are co-localized with ER proteins in astrocytes and that it might alter calcium dynamics. Such a co-localization could be crucial for calcium signaling, in particular in small volumes. We thus placed our study of the influence of calcium mobility on calcium signaling in a framework where calcium sources (IP_3R-dependent and IP_3R-independent) can co-localize.

To this end, the IP_3R-independent calcium influx in the cytosol (from e.g. plasma membrane transporters or channels) was made dependent on parameter R_γ, that sets the distance from IP_3R receptors within which new calcium ions are injected in the cytosol when they originate from IP_3R-independent fluxes (see Methods section). When $R_\gamma = 0$, the initial location of the new calcium ion is shared with an IP_3R channel whereas when R_γ increases, the injection positions of new calcium ions are increasingly uncorrelated from those of the IP_3R channels. When R_γ becomes as large as the size of the reaction surface (i.e. for $R_\gamma = 100$), the injection position of the new calcium ion is effectively independent of the positions of the IP_3R channels.

Our simulations show that the impact of the calcium diffusion coefficient is mainly visible when calcium sources are co-localized, i.e. for small values of R_γ. Fig 4A and 4B compare a representative simulation obtained when Ca^{2+} diffuses slowly (A) with a simulation obtained with perfectly-mixed calcium (B), in a case where the IP_3R receptors are not clustered ($\eta = 1$). Those representative simulations hint that the peak frequency is much larger with slow calcium, and suggests that slow calcium diffusion slightly favors the puff regime compared to perfect mixing. The systematic quantification of Fig 4C and 4D confirms these interpretations: when IP_3R-dependent and IP_3R-independent calcium sources are co-localized, i.e. for $R_\gamma < 5$, the value of D_{Ca} controls calcium transient frequency, as well as the probability to observe a puff. The effects are strong: for instance for $R_\gamma = 0$, decreasing D_{Ca} from 5 to 0.1 increases the frequency roughly threefold. However, when the IP_3R-independent influx was not co-localized with IP_3R channels (i.e. for $R_\gamma \geq 5$), both the peak frequency and the type of signal were found not to depend on the calcium diffusion coefficient anymore. Those results suggest that calcium diffusion could control the frequency and type of calcium signals within astrocytes when IP_3R channels are co-localized with IP_3R-independent calcium sources.
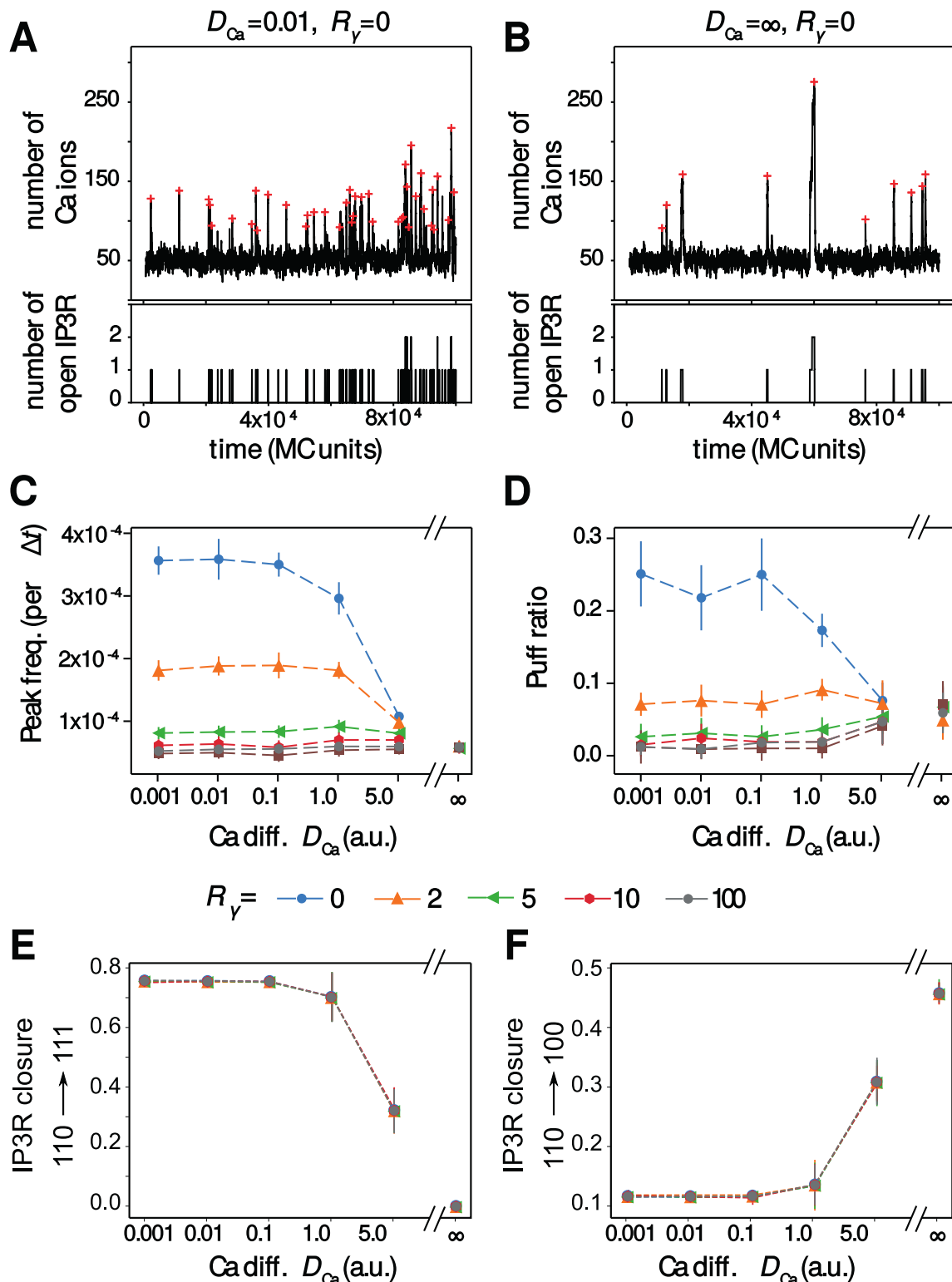
Fig 4. Ca²⁺ diffusion modulates the temporal characteristics of the signals upon co-localization. Representative simulations of the particle-based model showing both calcium trace and number of open IP_3R for co-localized calcium sources ($R_\gamma = 0$) in the case of slow calcium diffusion (*A*) or perfect-mixing of calcium (*B*). The red crosses show peak locations from automatic detection. The impact of calcium diffusion coefficient D_{Ca} on peak frequency (*C*) and the amount of puff (*D*) are shown for different values of the co-localization parameter R_γ: from $R_\gamma = 0$ (IP_3R are not clustered but co-localized with other calcium sources) to $R_\gamma = 100$ (IP_3R are neither clustered

nor co-localized). The puff ratio quantifies the fraction of peaks that are puffs. (E) and (F) respectively present the probabilities that IP_3R closure results from binding of a Ca^{2+} to the inactivating site (probability to switch to state {111}, $P_{110->111}$) or unbinding of an IP_3 (probability to switch to state {100}, $P_{110->100}$) depending on D_{Ca} and on R_γ. Probability of closure due to Ca^{2+} unbinding from activating site, $P_{110->010}$ can be deduced from $1 = P_{110->010} + P_{110->100} + P_{110->111}$. Data are presented as mean ± standard deviation over 20 simulations. Lines are guide for the eyes. Note that the x-axis scale in (C), (D), (E) and (F) is not regularly spaced. Other parameters: $\eta = 1$ (no clustering), $a_1 = 1$ a.u, $\mu = 50$ a.u.

Once open, i.e in state {110}, the IP_3R can switch to state {111} with probability $P_{110->111}$, due to binding of Ca^{2+} to the inactivating site. Open receptors can also switch to state {100} (or {010}) with probability $P_{110->100}$ (or $P_{110->010}$, respectively), due to the unbinding of IP_3 (or of Ca^{2+}, respectively) from the activating site. Fig 4E and 4F shows how the probabilities $P_{110->111}$ and $P_{110->100}$ vary with D_{Ca} and R_γ ($P_{110->010}$ can be deduced from $1 = P_{110->010} + P_{110->100} + P_{110->111}$). In contrast, R_γ has no significant effect on $P_{110->111}$, $P_{110->100}$ and $P_{110->010}$ probabilities. The effect of the effective diffusion coefficient D_{Ca} is strong: when low, most of IP_3R closure is due to the binding of Ca^{2+} to the inhibiting site. As D_{Ca} increases, $P_{110->111}$ decreases and in well-mixed conditions ($D_{Ca} = \infty$), IP_3R closure is always due to the stochastic unbinding of IP_3 and Ca^{2+}. So, receptor closure is strongly dominated by binding of Ca^{2+} to the inactivating site when Ca^{2+} effective diffusion is slow, but mostly relies on unbinding from the activating sites for fast Ca^{2+} effective diffusion. This result illustrates that well-mixed simulations are not well-suited to study the self-inhibiting behaviour of IP_3R, i.e the fact that the Ca^{2+} influx resulting from the opening of a given IP_3R can subsequently shut down this very receptor. Therefore accounting for diffusion with spatial models appears necessary to the study of the dynamics of IP_3R at the single-receptor scale.

IP_3R clustering controls calcium signals when co-localized

Experimental data demonstrate that IP_3R in SH-SY5Y and COS7 cells are not uniformly distributed on the ER membrane but form clusters [58, 59]. We next investigated the impact of IP_3R clustering on calcium signal dynamics in our particle-based model. Simulations were performed with $D_{Ca} = 0.1$ and various amounts of co-localization between IP_3R channels and other calcium sources (parameter R_γ). Representative simulations for uniformly-distributed IP_3R channels ($\eta = 1$) and strongly clustered IP_3R ($\eta = 50$) are presented in Fig 5A and 5B. In these two examples, the IP_3R were weakly co-localized with the IP_3-independent calcium sources (i.e. $R_\gamma = 10$). These traces indicate that the frequency and type of calcium signal in this case is heavily dependent on the spatial distribution of IP_3R channels: clustered IP_3R seem to exhibit much larger peak frequency and slightly more frequent puffs. However, here again this effect is quite mitigated by the amount of co-localization between IP_3R channels and the IP_3R-independent calcium sources. In particular, the dynamical range of the modulation by IP_3R cluster size η (i.e. the ratio between the frequency at $\eta = 50$ and $\eta = 1$) is maximal for intermediate co-localizations ($2 \leq R_\gamma \leq 10$) but the calcium peak frequency is hardly dependent on η when co-localization is either very strong ($R_\gamma < 2$) or very weak ($R_\gamma \geq 50$). Increasing clustering also tends to improve the emergence of puffs, although the effect is significant only for strong co-localization ($R_\gamma \leq 2$, Fig 5D). We emphasize that in such cases of strong co-localization, the regime of calcium activity (puffs vs blips) changes by simply rearranging the spatial distribution of the IP_3R, without changing any of the kinetics parameters of the model.

Taken together, these simulation results pinpoint the interplay between calcium source co-localization and the degree of IP_3R clustering as a crucial modulator of temporal characteristics of the calcium signals and of the signaling regime. In particular, they suggest that in the presence of certain amount of co-localization between IP_3R channels and other sources of calcium influx in the cytosol the spontaneous calcium peak frequency can have a large amplitude
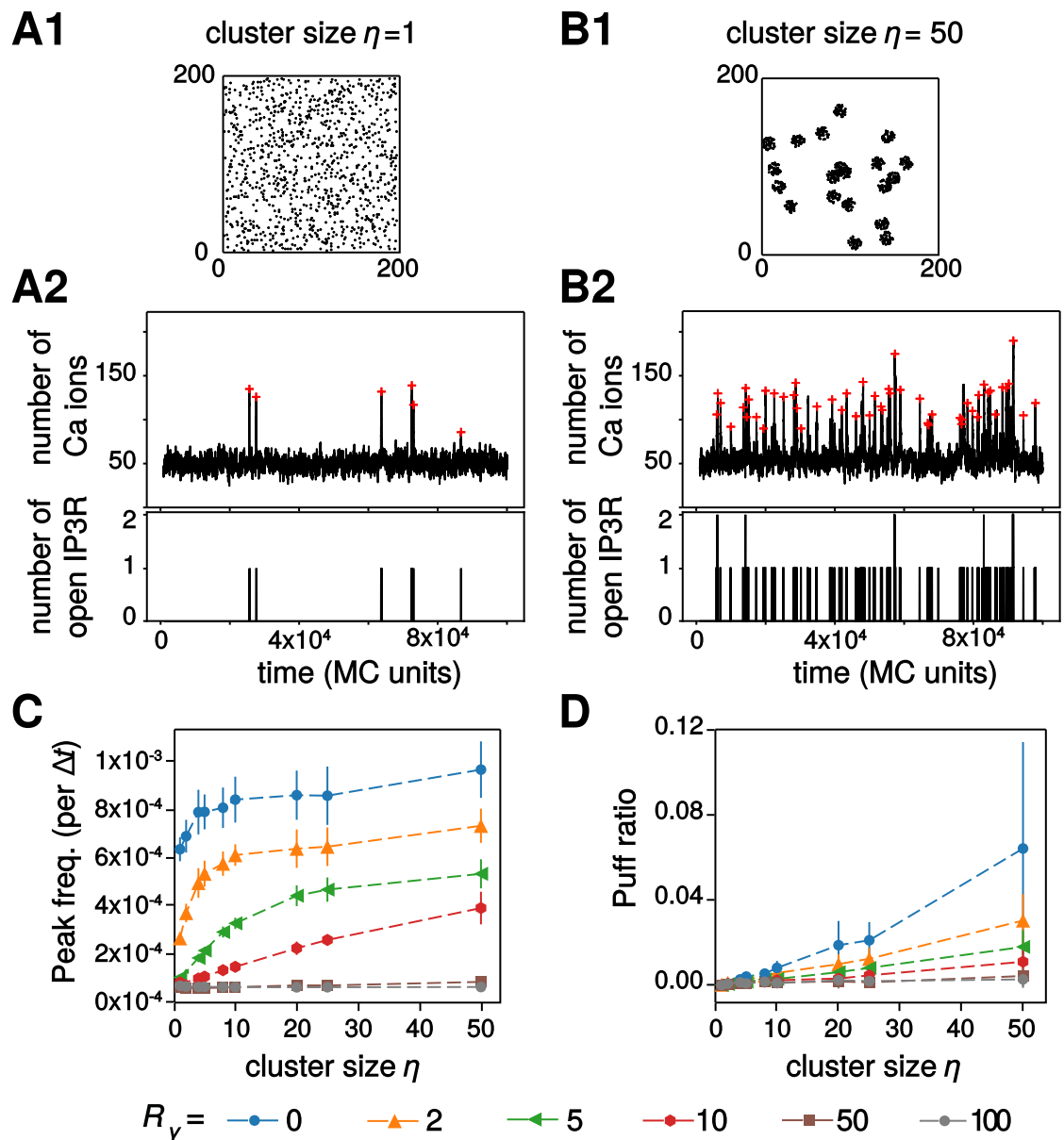
Fig 5. IP$_3$R clustering modulates calcium signals when co-localized. Representative simulations of the particle-based model with the corresponding IP_3R distribution over space, the calcium trace and number of open IP_3R for weakly co-localized calcium sources ($R_\gamma = 10$) in the case of uniform distribution of the IP_3R (A) or strongly clustered IP_3R (B) are illustrated. The red crosses show peak locations from automatic detection. The impact of IP_3R cluster size η on calcium peak frequency (C) and on the amount of puffs (D) are shown for different values of the cluster size: from $\eta = 1$ (IP_3R are not clustered) to $\eta = 50$ (strong clustering). Data are presented as mean ± standard deviation over 20 simulations. Lines are guide for the eyes. Other parameters: $D_{Ca} = 0.1$ a.u, $a_1 = 1$ a.u, $\mu = 50$ a.u.

variation. Within this range of parameters, calcium peak frequency can be finely tuned by the geometry of the colocalization.

Simulations in a compartmentalized 3d geometry reproduce spontaneous calcium microdomains signals

The above 2d simulations of the particle-based model have the advantage of a good computational efficiency, which makes them suitable for parametric studies with averaging over a

number of Monte-Carlo simulations. However, the 2d setting does not facilitate the comparison of the copy number of molecules in the simulations with species concentrations as measured experimentally. Moreover, it is difficult to investigate with a 2d setting the impact of the fact that IP_3R channels are specifically localized at the surface of the ER membrane and not freely diffusing in the cytosol bulk. To tackle those questions, we carried out simulations of our model in a more refined three-dimensional setting (Fig 6), in which we could adjust more precisely molecule concentrations, reaction volume and cytosol compartmentalization to what is expected in fine astrocytic processes. We then compared our simulations to experimental measurements of calcium dynamics in microdomains of comparable dimensions in mice hippocampal organotypic culture (Fig 6A). We have chosen to use organotypic slices as they provide better optical access and sample stability, which, combined with confocal microscopy, enabled us to distinguish individual processes (resolution $\approx$ 200 nm VS $\approx$ 500 nm with two-photon microscopy *in vivo*). While this resolution is not enough to resolve the exact sizes of PAPs, it provides the most realistic calcium dynamics experimentally available for calcium transients occurring at fine astrocytic processes.

As 80% of calcium activity occurs in astrocytic ramifications that cannot be resolved by optical microscopy [38], astrocytic calcium signaling models must take into account small volumes associated to it. For that purpose, we created the 3d structure mimicking one process geometry shown in Fig 6B. The reaction volume was chosen to match the range of sizes that are within reach of current imaging methods: a 1 μm-long cylinder of 100 nm radius (i.e. a volume around 0.03 fL), inside which we position a 0.75 μm-long cylindrical ER with a radius of 30 nm. In this 3d implementation, Ca^{2+} and IP_3 molecules diffuse in the bulk 3D space located between the external (plasma) membrane and that of the ER, while IP_3R molecules are distributed uniformly at random over ER membrane surface.

Our calcium imaging of calcium dynamics in fine astrocyte processes reveals the sponge-like structure of the processes Fig 6A1, with localized submicron calcium microdomains (regions of interest (ROI) in Fig 6A2) of size that can be less than $0.5\mu m^2$. The corresponding calcium traces display infrequent (a few hundredths of Hz) peaks with average amplitude around 2 ($\Delta F/F$) and typical duration of $\approx$ 2.7 seconds at FWHM (Fig 6A3 and 6D). Notice that these experimental traces correspond to spontaneous signals to the extent that they were measured in the absence of any neuronal or astrocytic stimulation. In particular, TTX application in this preparation did not alter peak frequency [69].

Our first noticeable result is that our model is able to reproduce the emergence of spontaneous calcium peaks of comparable frequency, duration and signal-to-noise ratio (Fig 6C). This result therefore indicates that spontaneous calcium signals can emerge in the fine processes even with a realistic basal calcium concentration of 83 ± 29 nM, which corresponds to only one to two calcium ions in the whole cylinder. Quantification of the free Ca^{2+} signal properties shows that signals are quantitatively and qualitatively different from experimental signals (Fig 6C and 6D, "No-GCaMP" simulations). Adding GCaMP6s to the model improved drastically both qualitatively and quantitatively the match between simulations and experimental data (Fig 6C and 6D, "GCaMP" and "GC+Buf" simulations), with no apparent difference between the "GCaMP" and the "GC+Buf" models. Note that our experimental statistics are tightly associated with the temporal sampling frequency used in the experiments (2 Hz) since very fast calcium events may be accessible only to higher sampling frequencies [38]. In particular, the experimental peak frequency measured might have been higher with better temporal resolution. Our spontaneous signals measured in organotypic hippocampal cultures are of the same order of magnitude as the ones measured *in vivo* [38, 70]. In any case, our results show that genetically encoded calcium indicators (GECIs), such as GCaMP6s, may change local calcium concentration, in particular close to open IP_3R channels, leading to an increased peak
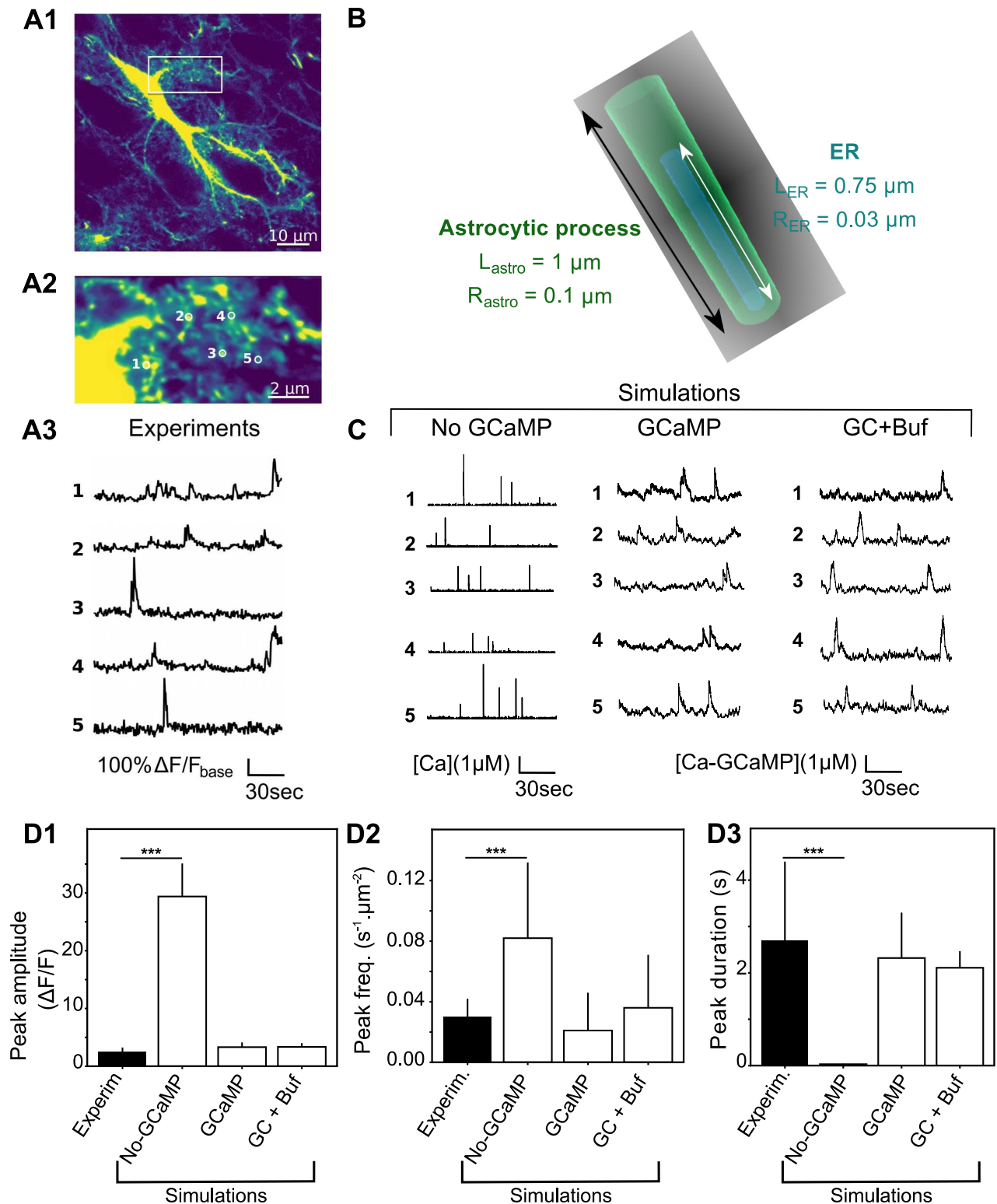
Fig 6. 3d model simulations in fine astrocyte processes successfully reproduce calcium microdomains signals. (*A*) Experimental monitoring of the spontaneous local Ca^{2+} signals in astrocytic sponge-like processes. Panel *A1* shows a 'summed projection' of a confocal time lapse image stack of a GCaMP6s-expressing astrocyte. Panel *A2* illustrates magnification of the boxed region of panel *A1*. Panel *A3* displays spontaneous calcium traces from the regions of interest shown in (*A2*). (*B*) The 3d geometry used for the 3D model is a cylinder of length $L_{astro} = 1$ *μm* and radius $R_{astro} = 0.1$ *μm*, with ER as a thinner cylinder inside. The interior volume is roughly 0.03 fL. (*C*) Representative simulations of calcium dynamics within the above cylinder

with the "No-GCaMP", "GCaMP" and "GC+Buf" simulations. The raw signal corresponds to cytosolic free calcium concentration for the "No-GCaMP" model and to calcium-bound GCaMP concentration for "GCaMP" and "GC+Buf" models. For all simulation types, parameter values were partly taken from the literature and partly adjusted for fitting calcium traces shown in *A* (reported in Table 2). (*D*) Quantitative comparisons of the spontaneous calcium signals measured experimentally (black bars) or simulated with the "No-GCaMP", "GCaMP" or "GC+Buf" models (white bars). The compared quantities are peaks amplitude in terms of $\Delta F/F$ ratio (D1), their frequency (measured in min^{-1} for each μm^2 area, D2) and duration (expressed as full width at half maximum, FWHM) D3. Significance is assigned by * for $p \leq 0.05$, ** for $p \leq 0.01$, *** for $p \leq 0.001$.

duration. Those results are in accordance with previous studies that demonstrate that calcium buffers, such as GECIs, modulate signal readout [53, 71].

Together these results demonstrate that our model, without any endogenous buffers, is enough to reproduce calcium signals within fine astrocytic processes in a quantitative way, making it a powerful tool to investigate calcium dynamics in the small volumes associated with PAPs.

Effect of GCaMP properties on calcium dynamics

Because our "GCaMP" simulations revealed that the use of GECIs may change local calcium concentration and thus impact peak duration, we have next investigated the effect on calcium dynamics of several parameters defining GCaMP molecules: their kinetics and their concentration. We tested to what extent using different GECIs in our simulations impacted calcium dynamics. We compared the dynamics of [GCaMP6s-Ca] with those of [GCaMP6f-Ca]. Although the total concentration of GECIs in those two models is identical, GCaMP6f-Ca signals display higher amplitude and smaller duration than GCaMP6s-Ca signals (Fig 7A1 and 7A3). Those results are partially in agreement with experimental measurements [72] that have reported a similar decrease of peak duration when using GCaMP6f compared to GCaMP6s. However, experimental observations also included a decrease of the peak amplitude with GCaMP6f, that we do not observe. This discrepancy could be due to a higher fluorescence baseline of GCaMP6f-Ca in those experiments, leading to decreased $\Delta F/F$ ratio.

As the concentration of GECIs cannot be controlled experimentally and is often not reported in calcium imaging studies, we have next investigated its effect on calcium signals (Fig 7B). Our simulations demonstrate that an increased GCaMP concentration in the cell results in a linear increase of basal GCaMP-Ca levels (Fig 7B1), with an unchanged basal concentration of free calcium. Increased [GCaMP] is associated with a decrease of GCaMP-Ca peak amplitude expressed in terms of $\Delta F/F$ ratio (Fig 7B2) and an increase of peak duration (Fig 7B4). Interestingly, varying [GCaMP] does not seem to have an impact on peak frequency (Fig 7B3), which is contradictory to Skupin et al's results that have demonstrated a non-linear increase of the average signal period with the concentration of exogenous buffers [54]. However, Skupin et al studied whole-cell EGTA or BAPTA dynamics, which is fundamentally different from the local spontaneous GCaMP-Ca signals in the fine processes that we are modelling here. Local variations of cellular GCaMP concentration might thus yield variations of peak duration and amplitude, so that measuring cellular GCaMP concentration and its variations along the cellular compartments appears crucial to analyze calcium signals more accurately.

Discussion

Recent experimental reports suggested that the complete dependence of cytosolic calcium transients on IP_3R2 is only observed in the astrocyte cell body whereas calcium signals measured within astrocytic processes are a mix of IP_3R2-dependent and non-IP_3R2-dependent
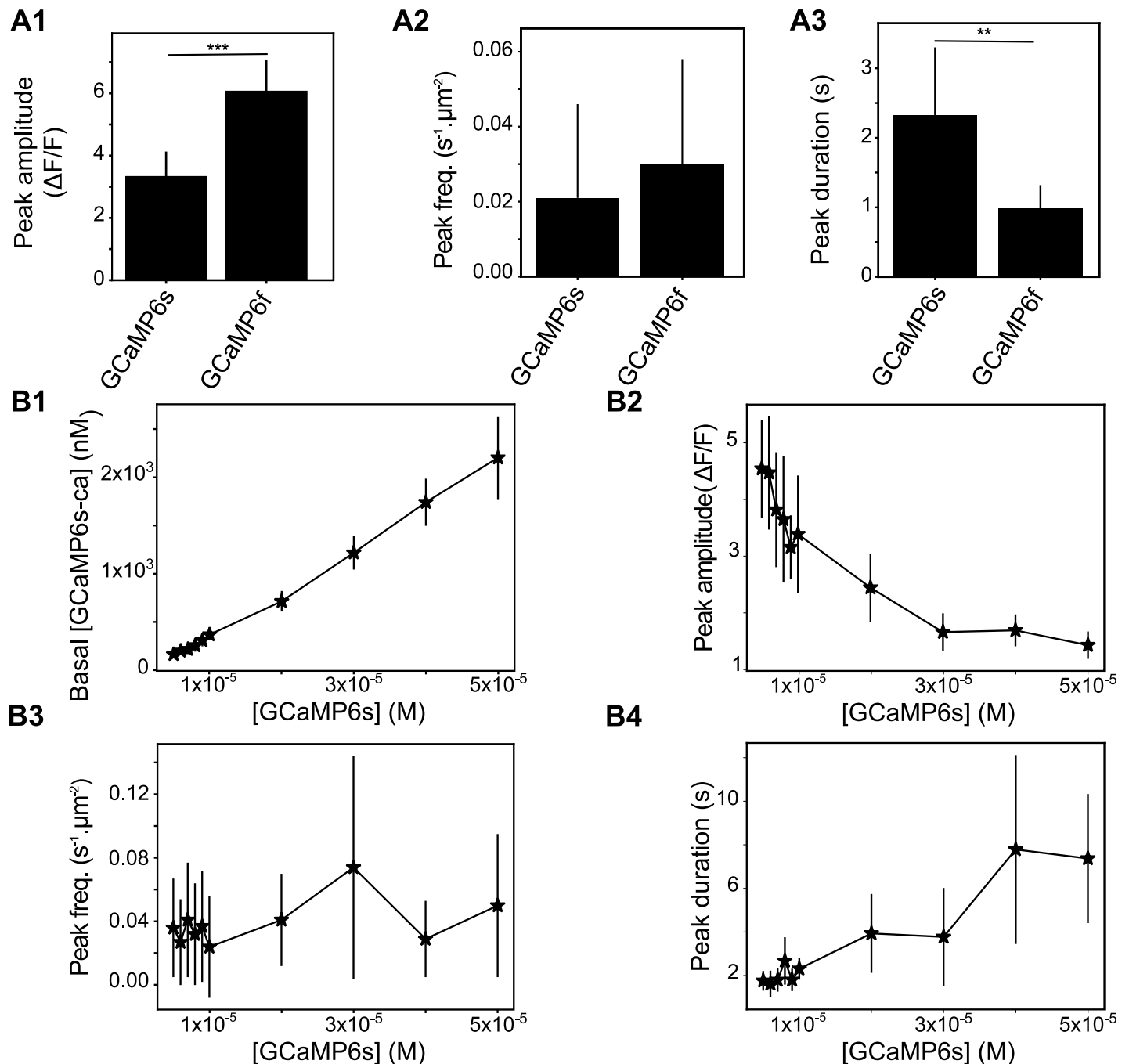
Fig 7. The kinetics and concentration of GECIs strongly influence calcium dynamics. (*A*) Quantitative comparisons of the spontaneous calcium signals measured with "GCaMP6s" or "GCaMP6f" as fluorescent reporters. The compared quantities are peak amplitude in terms of $\Delta F/F$ ratio (A1), frequency (measured in min^{-1} for each μm^2 area, A2) and duration (expressed as full width at half maximum, FWHM) (A3). (*B*) The impact of the concentration of GCaMP6s in the system on basal concentration of GCaMP-Ca (B1), on the GCaMP-Ca peak amplitude (B2), frequency (B3) and duration (B4) are shown for different values of [GCaMP6s]. Significance is assigned by * for $p \leq 0.05$, ** for $p \leq 0.01$, *** for $p \leq 0.001$. Data are presented as mean ± standard deviation over 20 simulations. Lines are guide for the eyes.

https://doi.org/10.1371/journal.pcbi.1006795.g007

calcium signals [21, 28]. The identity, subtype and localization of the receptors responsible for non-IP_3R2-dependent calcium signals in astrocytes, in particular their processes, are still to be uncovered. However, our study sheds light on the importance of the localization of these various calcium sources. Our simulation results indeed indicate that when IP_3R

channels are (even moderately) co-localized with IP_3R-independent calcium sources, e.g. plasma membrane calcium channels, the degree of IP_3R clustering and/or the mobility of the calcium buffers will have a strong impact on the frequency and amplitude of the spontaneous calcium signals. In particular, our simulations predict that two astrocyte processes expressing exactly the same repertoire of channels, pumps and receptors but in a different spatial organization (for instance various degrees of clustering or co-localization), can exhibit very different types and properties of spontaneous calcium events. This could result in significant variability of the calcium response of different processes, even from the same cell. Moreover, our results suggest that 'puffs' might reflect cellular sub-compartments in which calcium channels are co-localized, which increases the calcium response to a given stimulus. It would thus be interesting to investigate whether those co-localizations can be observed at specific locations, such as at neuron-astrocyte contact sites, or if they are randomly distributed within the cell.

During the past few years, fine astrocytic processes have been regarded as devoid of ER [73, 74]. This questions the validity of our model, in which the presence of ER-attached IP_3R in the process is crucial for spontaneous activity. We however note that a recent EM study has observed that ER dynamically ramified in astrocyte perivascular processes *in vivo* and detected contact sites between ER processes and plasma membrane, often positioned in apposition to neuronal synapses [75]. Such contiguous membranous juxtapositions would definitely validate the presence of ER in PAPs. Although dynamical ER remodeling has been reported in dissociated astrocyte culture [76], technical limitations have prevented direct investigation of ER localization within PAPs *in vivo* or in slices. To our knowledge, it is not even clear whether astrocytic ER is continuous or consists in several independent reservoirs. Super-resolution microscopy of cellular ER and mitochondrial dynamics and structure (resolution $\approx$ 100nm) has recently been developed and could help solve the controversy regarding the presence of ER in fine processes [77, 78]. Correlative super-resolution fluorescence imaging and electron microscopy approaches can yield a resolution of less than 50 nm (down to 10nm) [79], which is very promising avenue to PAPs ultrastructure investigation. ER-bound GECIs, OER-G-CaMP6f, have been recently developed and, combined with the use of ER luminal calcium indicators such as G-CEPIA1$_{er}$ [80], could help investigate the involvement of calcium channels on the ER membrane in calcium dynamics depending on subcellular localization in astrocytes [81]. In any case, since the IP_3R pathway is involved in calcium dynamics, further investigations regarding ER sub-cellular localization, sub-compartmentalization and dynamics are crucial for better understanding astrocyte information processing. Meanwhile, a straightforward extension of our computational model would be to simulate neuronal stimulation-triggered calcium dynamics.

IP_3Rs are thought to assemble as tetramers, and a recent experimental study suggested that the four subunits of the tetramer must be simultaneously bound to IP_3 for the tetramer to allow calcium influx, independently of cytosolic calcium or ATP concentrations [82]. Actually, the original IP_3R model predicted that subunit cooperativity for calcium binding is also necessary to fit experimental data of IP_3R dynamics [46, 48]. Even though the IP_3R binding sites for calcium have been characterized, their roles in IP_3R dynamics are still poorly understood [83]. The requirement for inter-subunit cooperativity, in which the 4 IP_3 binding sites should simultaneously be bound for the tetramer to open, is expected to hinder the emergence of spontaneous calcium events. In a subset of simulations, we have replaced our non-cooperative IP_3R model, in which the binding of a single IP_3 site is enough to open the monomer channel, with the cooperative model proposed by Bicknell and collaborators [84]. With 100 nM basal IP_3 and Ca^{2+} [85, 86], we could not produce spontaneous calcium signals in these conditions, even after a search of the parameter space to locate parameters allowing spontaneous activity with

this cooperative model. This issue might reflect a general problem of the De Young Keizer model in discrete particle-based models with low copy number of particles. The De Young Keizer model is based on steady-state experimental data representing averages over time and over channel populations, which proved sufficient to reproduce experimental statistics such as the average open time or the steady-state open probability. However, this model might not be suited to describe behaviors at the level of individual channels and low copy number of particles. More recent models have been proposed that successfully reproduce the evolution with time of the open/close dynamics of a single IP_3R [87, 88]. In those models, the transition rates between different states of the IP_3R are not triggered by Ca^{2+} or IP_3 binding events but by complex continuous functions of their concentrations. We could not implement such complicated functions with a pure particle-based modeling strategy such as used here. Therefore, further investigations are needed to clarify the suitability of the De Young Keizer model in the context of particle-based spatially-explicit stochastic models. Alternatively, our results may be interpreted as casting doubts on the existence of spontaneous calcium signals in astrocytes when the basal IP_3 and Ca^{2+} concentrations are of the order of 100 nM. A number of studies have reported higher calcium concentration localized at the vicinity of calcium channels [89–91]. Such calcium microdomains, in the vicinity of IP_3R, could facilitate the emergence of spontaneous signals from cooperative IP_3Rs in thin processes.

On the other hand, experimental evidence for spontaneous calcium signals in astrocytes is still debated. Even in the absence of presynaptic neural activity, presynaptic axon terminals do probabilistically release neurotransmitter vesicles, generating so-called miniature EPSCs. Bafilomycin application has been used in several experimental studies to investigate the dependence of astrocytic calcium signals on EPSCs, because this inhibitor of V-ATPases inhibits miniature EPSCs by blocking the refill of presynaptic vesicles. However, the impact of bafilomycin bath application on the frequency of spontaneous calcium signals in astrocytes has proven variable (compare e.g. [92] and [93]). In our preparation, bath-application of bafilomycin strongly decreased peak frequency and amplitude [69]. As bafilomycin has a wide range of effects on calcium signaling that is independent of its effect on the refill of presynaptic neurotransmitter vesicles [94, 95], we cannot conclude whether those signals are triggered by EPSCs and further investigation is needed to decipher whether the "spontaneous" calcium signals reported in astrocyte processes are due to spontaneous release of presynaptic vesicles or rely on a synapse-independent mechanism inherent to the CICR system.

For simplicity, IP_3R clustering in our model was considered static during simulation time. Experimentally, though, IP_3R clustering might be highly dynamic [96, 97]. Several molecules can trigger IP_3R clustering, including IP_3 and calcium themselves [96, 97], through a mechanism that may include the lateral diffusion of IP_3R on the ER surface [97] or be independent from it [98]. Beyond this IP_3R classification into clustered and un-clustered populations, another approach is to quantify single IP_3R channels based on their mobility. A recent study on HeLa cells [41] indicates that calcium signals emerge most of the time from immobile IP_3R, which are found in apposition to ER-plasma membrane junctions, whereas the mobile IP_3R fraction would not be involved in calcium influx. Our simulation results, in agreement with previous IP_3R-mediated calcium models [99, 100], indicate that IP_3R clustering can lead to an increase of the frequency and amplitude of their calcium signals. This result is in contradiction with a previous modeling study that concluded in favor of a reduction of IP_3R channel activity upon IP_3R clustering [101]. This discrepancy might rely on the different modeling choices. In particular, the model in [101] incorporates a 5-state IP_3R model derived from Tu et al. [102, 103]. All of those modeling studies however agree that dynamical IP_3R clustering could be a mechanism used by astrocyte processes to modulate their calcium signals. This could provide astrocyte processes with a capacity for information processing plasticity.

In our model, the value of the rate constant for calcium binding on IP_3R changes the type of spontaneous dynamics (e.g. blips vs puffs) in addition to its characteristics (frequency, amplitude). Experimentally, several post-transcriptional mechanisms can modulate IP_3R affinity. For instance, phosphorylation of type-1 and -2 IP_3R by cAMP-activated PKA increases the affinity of IP_3R to calcium and IP_3 [104]. At a larger time scale, the sensitivity of IP_3R to calcium is encoded in a sequence of calcium sensor (Cas) region that differs depending on the IP_3R isoform [102, 105, 106]. Since multiple IP_3R isoforms seem to be involved in calcium signaling within astrocytic processes [33], they could assemble into a variety of homo- or hetero-IP_3R tetramers that would exhibit a range of calcium and IP_3 affinity.

In addition, immobile or weakly mobile endogenous calcium buffers are responsible for an effective intracellular calcium diffusion that is an order of magnitude slower than free calcium ions [107]. Our simulation results indicate that the value of the effective Ca^{2+} mobility also participates in the determination of the type and characteristics of the spontaneous events, thus confirming previous experimental [108] and modeling studies [53, 60, 62, 109, 110]. Although our simulations with both GCaMP and endogenous buffers,"GC+Buf", overall displayed dynamics similar to the simulations without endogenous buffers ("GCaMP"), we note that, similarly to the effect of GCaMP concentration, increasing the concentration of endogenous buffers led to longer duration of the calcium signals. Those results are consistent with previous studies that have demonstrated significant effects of buffers [61] or of intra-cluster channel communication and coupling [53] on calcium dynamics. Endogenous calcium buffers display various kinetics and diffusion coefficients in astrocytes [111] and some of them are overexpressed in hippocampal and striatal astrocytes, possibly in a region-specific pattern [112], which could be involved in the regional variability of astrocytic calcium signals [113]. Our study shows that precisely accounting for the effects of GECIs and endogenous calcium buffers on calcium dynamics is crucial for better interpreting calcium signals in PAPs. Particular care should be taken when interpreting GCaMP-Ca signals as GCaMP concentration is rarely monitored although it could be partly responsible for the diversity of calcium signals observed in PAPs.

Therefore, in addition to the spatial organization of the Ca^{2+} channels, the differential expression of endogenous calcium buffers, including the fluorescent Ca^{2+} reporters, could also be potential determinants allowing a range of responsiveness and spatio-temporal characteristics of calcium signals in astrocyte processes.

To conclude, we have presented a spatially-explicit stochastic model to investigate intracellular calcium signaling based on CICR in small sub-cellular volumes. Recent studies proposed models for the simulation of astrocytic sodium [114] and calcium signals [74, 115, 116] in 3d with deterministic differential equation models that correspond to cellular volumes large enough to validate a law of large numbers. To our knowledge, our model is the first model suited to reproduce spontaneous calcium signals in the finest astrocyte processes, where low copy number and spatial localization effects are expected to be more prominent than in larger volumes. Our simulations demonstrate that low copy number of molecules can display dynamics that cannot be predicted by deterministic approaches and that spatial modelling is crucial to better understand the effect of molecular distributions and sub-compartments geometries on calcium dynamics. Since these fine processes are thought to be the place of initiation of neuron-astrocyte interactions, we believe that this model, combined with models of signal propagation between astrocytic compartments such as Savtchenko et al. [116], might be useful to investigate the initiation and spatiotemporal integration of calcium signals in the sponge-like network of astrocyte processes, a prerequisite to understand neuron-astrocyte communication.

Materials and methods

Modeling methods

Reaction scheme. The model considers cytosolic calcium and IP_3 dynamics in the framework of calcium-induced calcium release (CICR) signaling. The reaction scheme considered is shown in Fig 1 A. In short, we consider calcium fluxes between the cytosol and the extracellular space or the endoplasmic reticulum (ER), including via IP_3R channels. We also take into account the effect of phospholipase C δ (PLCδ), that, when activated by calcium, synthesizes IP_3. To derive simple models for this scheme, we made the following assumptions:

- We considered that the extracellular and ER calcium concentrations are constant during the simulation, as well as the electrical potentials across the plasma and ER membranes. In this case, calcium outflow from the cytosol to the ER or to the extracellular medium can be lumped into a single first-order rate α. Likewise, calcium entry from the extracellular medium or any IP_3R-independent Ca^{2+} influx from the ER can be considered constants, too. We lumped them into a single overall constant flux γ.

- PLCδ enzymes remain located in the cytosol (no translocation) and the amount of their substrate PIP2 is present everywhere in large excess. Under this condition, activated PLCδ produces IP_3 with constant rate δ.

IP_3R channels are gated both by calcium and IP_3, with a bell-shaped dependence of the open probability to calcium concentration [56]. To model their dynamics, we used the classical 8-state Markov model proposed in [46, 56], with two calcium binding sites, referred to as 'Ca sites', and one IP_3 binding site for each IP_3R (see Fig 1B). However we used the following simplifications:

- We considered that the binding or unbinding rate constant of a given binding site is independent from the occupancy state of the other sites (no intra-channel cooperativity). Under this assumption, the rate constant for calcium binding at the first calcium binding site, a_1, does not depend on whether the other two binding sites are bound or not. Thus, the rate constant for $\{000\} + Ca \rightarrow \{100\}$ has the same value as e.g. the reaction $\{011\} + Ca \rightarrow \{111\}$ (where the triplet notation corresponds to the one defined in Fig 1). Likewise, the rate constants for Ca^{2+} or IP_3 binding or unbinding to the three sites were considered independent from the other occupancy states.

- The open state is assumed to be state $\{110\}$ (first Ca site and IP_3 bound, second Ca site free), as in [46, 56]. These latter models further assume inter-channel cooperativity, where IP_3R channels assemble as tetramers of which at least three monomers must be in the open state for calcium to be transferred. Here we neglected inter-channel cooperativity and considered that every single channel was open when in the open state i.e., as long as an IP_3R channel is open, it is assumed to inject calcium in the cytosol at constant rate μ.

Monte Carlo simulations of the spatially-explicit stochastic particle-based model. We first modeled the kinetic scheme described in Fig 1 with a lattice-free spatially-explicit stochastic particle-based model, referred to as "Particle-based" model below, in two spatial dimensions, with reflective boundary conditions. Each molecule of the system was explicitly modeled with its associated position in space. PLCδ and IP_3R molecules were considered immobile whereas Ca^{2+} and IP_3 molecules were mobile by diffusion. At the beginning of each Monte-Carlo (MC) simulation of this model, the space coordinates for each Ca^{2+}, IP_3 and PLCδ molecules are chosen uniformly at random.

To determine the positions of the N_{IP_3R} IP_3R molecules, we first chose the centers of $N_c = N_{IP_3R}/\eta$ IP_3R clusters uniformly at random in the reaction space, where η is the number of

IP_3R per cluster (as illustrated in Fig 1C). For each cluster, we positioned η IP_3R molecules uniformly at random within a distance R_c of the cluster center, with $R_c = d_{IP_3R} \sqrt{\eta/0.91}$, where d_{IP_3R} is the interaction distance of the IP_3R, i.e. the maximal distance between IP_3R center and a Ca^{2+} or IP_3 molecule below which binding can occur. According to this algorithm, $\eta = 1$ corresponds to randomly distributed independent IP_3R molecules (no clustering) whereas IP_3R molecules become increasingly clustered when η increases, with constant IP_3R density within the clusters and constant total IP_3R number in the reaction space.

Each MC stimulation step (of duration Δt) consists in iterating the following steps:

1. *Diffusion.* The position of each mobile molecule (Ca^{2+} and IP_3) is updated independently according to Brownian motion: $\mathbf{r}(t + \Delta t) = \mathbf{r}(t) + \sqrt{2D_i \Delta t}\xi$, where D_i, $i = \{Ca, IP3\}$ is molecule i diffusion coefficient and ξ is a vector of i.i.d. Gaussian-distributed random numbers with zero mean and unit variance. In a subset of simulations, the new position of each mobile molecule was chosen at random in the reaction volume, i.e. $\mathbf{r}(t + \Delta t) = \zeta$ were ζ is a vector of i.i.d. random numbers uniformly distributed in $[0, L]$, with L the length of the spatial domain. We refer to this setting as "infinite" diffusion coefficients, $D = \infty$.

2. *Binding.* For each Ca^{2+} ion close enough to a PLCδ to react (i.e. when the distance between both is less than the interaction radius of PLCδ), a new IP_3 molecule is created with probability $\delta\Delta t$ at the position of the PLCδ molecule. Likewise, each Ca^{2+} or IP_3 molecule close enough to an IP_3R molecule (i.e. within its interaction radius) can bind it depending on its occupancy state. If the IP_3 binding site is free, an IP_3 molecule binds with probability $a_2\Delta t$. If one of the Ca sites is free, a Ca^{2+} ion binds the free site with probability $a_1\Delta t$ (first Ca site) or $a_3\Delta t$ (second Ca site). If both Ca sites are free, binding occurs to the first site with probability $a_1\Delta t$ and to the second one with probability $(1 - a_1\Delta t)a_3\Delta t$.

3. *Unbinding.* Each IP_3R molecule releases its bound Ca^{2+} or IP_3 molecules independently, with probability $b_1\Delta t$ (first Ca site), $b_2\Delta t$ (IP_3 site) and $b_3\Delta t$ (second Ca site). Ca^{2+} or IP_3 molecules that bound the IP_3R at the previous (binding) step of the current time step do not unbind.

4. *Removal.* Free cytosolic Ca^{2+} and IP_3 molecules are removed from the cytosol with probability $\alpha\Delta t$ and $\beta\Delta t$, respectively. Ca^{2+} and IP_3 molecules that unbound from IP_3R at the previous (unbinding) step of the current time step are not removed.

5. *Ca^{2+} Influx.* For each IP_3R channel in the open state {110}, a new Ca^{2+} ion is created in the cytosol at the IP_3R position with probability $\mu\Delta t$. A new calcium ion can also be created in the cytosol with probability $\gamma\Delta t$, mimicking Ca^{2+} influx from IP_3R-independent sources in the ER membrane or through the plasma membrane. Note that the position of this new calcium is not uniform over space but depends on parameter R_γ and works as follows: an IP_3R molecule is chosen (uniformly) at random and the new Ca^{2+} ion is positioned uniformly at random within distance R_γ of the chosen IP_3R. Therefore low values of R_γ emulate co-localization between IP_3R-dependent and IP_3R-independent Ca^{2+} influx sources, whereas the location of IP_3R-independent Ca^{2+} influx is uniform over the reaction volume when R_γ becomes as large as the volume side length.

Table 1 gives the parameter values used in our 2D simulations, including the initial numbers of Ca^{2+}, PLCδ, IP_3 and IP_3R molecules.

Mean-field (MF) dynamics of the perfectly stirred model. With infinite diffusion, the dynamics of the system can be assumed to be perfectly stirred. With that mean-field (MF) assumption, the temporal dynamics of reaction scheme Fig 1 can be modeled using ordinary

differential equations based on the mass-action law. IP_3R dynamics in these conditions can be described with seven ODEs that express the temporal dynamics of the concentration of IP_3R in state $\{ijk\}$, $[ijk]$:

$$
\begin{cases}
\mathrm{d}[000]/\mathrm{d}t = -(a_1[Ca] + a_2[IP3] + a_3[Ca])[000] + b_1[100] + b_2[010] + b_3[001] \\
\mathrm{d}[001]/\mathrm{d}t = -(a_1[Ca] + a_2[IP3] + b_3)[001] + b_1[101] + b_2[011] + a_3[Ca][000] \\
\mathrm{d}[010]/\mathrm{d}t = -(a_1[Ca] + b_2 + a_3[Ca])[010] + b_1[110] + a_2[IP3][000] + b_3[011] \\
\mathrm{d}[011]/\mathrm{d}t = -(a_1[Ca] + b_2 + b_3)[011] + b_1[111] + a_2[IP3][001] + a_3[Ca][010] \\
\mathrm{d}[100]/\mathrm{d}t = -(b_1 + a_2[IP3] + a_3[Ca])[100] + a_1[Ca][000] + b_2[110] + b_3[101] \\
\mathrm{d}[101]/\mathrm{d}t = -(b_1 + a_2[IP3] + b_3)[101] + a_1[Ca][001] + b_2[111] + a_3[Ca][100] \\
\mathrm{d}[110]/\mathrm{d}t = -(b_1 + b_2 + a_3[Ca])[110] + a_1[Ca][010] + a_2[IP3][100] + b_3[111]
\end{cases}
\tag{1}
$$

where $[Ca]$ and $[IP3]$ denote Ca^{2+} and IP_3 concentration, respectively. The concentration of the eighth occupancy state, $\{111\}$ is obtained from conservation of the IP_3R, i.e. $[111] = N_{IP_3R}/V - ([000] + [001] + [010] + [011] + [100] + [101] + [110])$. IP_3 dynamics in the mean-field model is given by:

$$
\mathrm{d}[IP3]/\mathrm{d}t = -a_2[IP3]\sum_{i=0}^{1}\sum_{k=0}^{1}[i0k] + b_2\sum_{i=0}^{1}\sum_{k=0}^{1}[i1k] + \delta[PLC\delta][Ca] - \beta[IP3]
\tag{2}
$$

where $[PLC\delta] = N_{plc}/V$. Finally, the mean-field dynamics of the free Ca^{2+} is obtained with:

$$
\begin{aligned}
\mathrm{d}[Ca]/\mathrm{d}t = \ & -\left(a_1\sum_{j=0}^{1}\sum_{k=0}^{1}[0jk] + a_3\sum_{i=0}^{1}\sum_{j=0}^{1}[ij0]\right)[Ca] \\
& + b_1\sum_{j=0}^{1}\sum_{k=0}^{1}[1jk] + b_3\sum_{i=0}^{1}\sum_{j=0}^{1}[ij1] \\
& - \alpha[Ca] + \gamma + \mu[110]
\end{aligned}
\tag{3}
$$

For comparison with the output of the other models, the concentrations were transformed into numbers of molecules by multiplication by the reaction volume V.

Perfectly-stirred stochastic temporal dynamics (SSA). For comparison, we also modeled the reaction scheme depicted in Fig 1 using Gillespie's exact Stochastic Simulation Algorithm (SSA) that accounts for stochasticity due to low copy numbers and assumes perfect mixing of the reactants [117, 118]. Here, the dynamic variables are the number of Ca^{2+} and IP_3 molecules in the system, N_{Ca} and N_{IP3} and the number of IP_3R channels in state $\{ijk\}$, N_{ijk}. The rates of all the reactions of the scheme of Fig 1 are then calculated according to mass-action laws like in the MF model of Eqs (1), (2) and (3). For instance, at reaction time t, the rate of reaction $\{001\} + Ca \rightarrow \{101\}$ is given by $a_1/V\, N_{001}(t)N_{Ca}(t)$. The next reaction time τ is sampled from an exponential distribution with mean $1/R_T$, where R_T is the sum of the reaction rates of all reactions. The next reaction to occur at time $t + \tau$ is chosen as an integer random variable with point probability given by the ratio of its rate to R_T. For instance, for the reaction illustrated above, the probability that this reaction is the one occurring at time $t + \tau$ is $a_1/V\, N_{001}(t)N_{Ca}(t)/R_T$. Finally, the variables are updated according to the chosen reaction. In the data presented below, we have modeled each receptor individually, i.e. for each receptor $l \in 0\dots N_{IP_3R}$, $N_{ijk}^l = 1$ if receptor l is in state ijk, 0 else. If the illustration reaction described above on receptor l is chosen, this means $N_{001}^l(t + \tau) = N_{001}^l(t) - 1$, $N_{Ca}(t + \tau) = N_{Ca}(t) - 1$ and $N_{101}^l(t + \tau) = N_{101}^l(t) + 1$. The other variables keep their values.

Realistic simulations in 3d astrocytic processes. In order to simulate calcium dynamics within a more refined 3d geometry with realistic volumes and concentrations, we built a

model in STEPS (http://steps.sourceforge.net/). STEPS is a software for voxel-based stochastic reaction-diffusion simulations within complex 3d geometries that simulates stochastic chemical reaction-diffusion with a spatialized version of Gillespie's SSA, usually referred to as the reaction-diffusion master equation (RDME). In RDME, space is partitioned into voxels inside which perfect mixing is assumed, while diffusion between adjacent voxels is modeled as first order reactions [119, 120]. STEPS uses a derivative of the SSA in tetrahedral voxels that allows for a better resolution than the cubic voxels mostly used in voxel-based models [121].

Geometry. The main advantage of STEPS in the context of the present study is its automatic handling of external and internal membranes [122]. Moreover, STEPS simulations can easily be parallelized [123], a crucial property given the computational burden of such compartmentalized 3d simulations. This allowed us to explicitly describe the presence of the ER membrane inside the 3d cell cytoplasm and the fact that IP_3R channels are located in the ER membrane. The geometry of the reaction volume consisted in a cylinder of length $L_{astro} = 1\ \mu$m and radius $R_{astro} = 0.1\ \mu$m. The ER was modeled as a second cylinder, internal, with length $L_{ER} = 0.75\ \mu$m and radius $R_{ER} = 0.03\ \mu$m. The resulting cytosolic volume (2.81×10^{-17} L) was meshed with 11345 tetrahedra of individual volume $2.48 \times 10^{-21}\ L$, thus ensuring the well-mixed subvolume condition [121].

Reactions. In this spatial configuration, we modeled the IP_3R-mediated calcium signaling kinetic scheme of Fig 1 with IP_3R channels positioned on the intracellular ER membrane and according to three model variants:

- A first variant, referred to as the "No-GCaMP" model, did not include fluorescent calcium indicators. In this 3d model, parameter values were taken, whenever possible, from the literature (Table 2). γ and α values were adjusted to yield basal calcium concentration around 120 nM [86, 124]. Likewise, β and μ were adjusted for a basal IP_3 concentration of 120nM [85]. Note that this value is based on recent, precise measurements of IP_3 concentration and differs by an order of magnitude from IP_3 concentration values routinely used in IP_3R-mediated calcium models [59, 125, 126]. IP_3R density on the ER surface has been measured from TIRF-microscopy analysis in cell cultures [89], reporting IP_3R cluster diameters of 0.3 μm at most, with up to 10 IP_3R per cluster. The ER surface area in our model is 0.69 μm^2. Ignoring the potential unclustered IP_3Rs [98], this represents a maximum of 4 clusters, thus at most 40 IP_3R. We thus set the number of IP_3R in our model to 50 channels on the ER surface. Finally, Ca^{2+} and IP_3 binding and dissociation constants to IP_3R were adjusted to fit our experimental data of calcium micro-domains in organotypic cultures of hippocampal astrocytes.

- A second variant of the 3d model, referred to as the "GCaMP"(="GCaMP6s") model, was obtained by adding GCaMP6s calcium indicators in the cytosol. GCaMP6s are ultrasensitive calcium indicators that fluoresce when bound to Ca^{2+}. The fluorescence signal from experimental data indeed corresponds to the concentration of calcium-bound GCaMP6s, which can be quite different from free cytosolic Ca^{2+} trace. For this model, all the parameters were set to the same values as the "No-GCaMP" model, except those related to GCaMP that were taken from the available experimental literature and shown in Table 2. The parameters for GCaMP6f kinetics were taken from Chen et al. [72].

- A third variant of the 3d model, referred to as the "GC+Buf" model, was obtained by adding endogenous buffers to the "GCaMP" model. The kinetic scheme is presented in S2 Fig. Parameter values for calcium, IP$_3$, IP$_3$R and GCaMP dynamics were the same as the "GCaMP" model. Parameter values for endogenous buffers dynamics were taken from the literature [127] and are presented in S1 Table.

Table 2. Parameter values and initial conditions of the 3d model. The parameter values for the 3d model listed here correspond to the "GCaMP" model. The parameter values for the "No-GCaMP" 3d model are the same except that GCaMP6s concentration equals 0 nM. In the "GCaMP6f" model variant, $Gcamp_f = 1.05 \times 10^7\ M^{-1}.s^{-1}$ and $Gcamp_b = 3.93 s^{-1}$. Parameter values in the 3d model have been adjusted to optimize the match with experimental data as described in the Methods section. Note that the values for calcium and IP_3 binding or unbinding to IP_3R, i.e. the a_i's and b_j's parameters below, are smaller in our model than in the literature, probably because our model is not cooperative. For GCaMP6s and GCaMP6f, we used the diffusion coefficient of calmodulin. The initial number of Ca^{2+} ions was adjusted so that the measured basal GCaMP6s-Ca concentration was around 300nM [86, 124].

Parameter	Description	Value in 3d GCaMP model	Reference
V	Cell volume	2.81×10^{-17} L	[128]
		IP_3 dynamics	
IP_0	Initial IP_3 number/conc	3 molec. i.e 177 nM	[85]
D_{IP3}	IP_3 diffusion	280 $\mu m^2.s^{-1}$	[107]
N_{plc}	PLCδ number/conc.	1696 molec. i.e 100 μM	[129]
δ	PLCδ max rate	1 s^{-1}	-
β	IP_3 decay	$1.2 \times 10^{-4}\ s^{-1}$	-
		Ca^{2+} dynamics	
Ca_0	Initial Ca^{2+} number/conc.	5 molec. i.e 295 nM	[86]
D_{Ca}	Ca^{2+} diffusion	13 $\mu m^2.s^{-1}$	[107]
μ	Ca^{2+} flux through open IP_3R	$6 \times 10^3\ s^{-1}$	-
γ	cytosolic Ca^{2+} influx	$1.5 \times 10^{-7}\ s^{-1}$	-
α	Ca^{2+} decay rate	30 s^{-1}	-
		GCaMP6s	
C_{GCa}	GCaMP6s conc.	169 molec. i.e 10 μM	[130, 131]
D_{GCaMP}	GCaMP6s diffusion	50 $\mu m^2.s^{-1}$	[132]
$Gcamp_f$	GCaMP6s Ca binding rate	$7.78 \times 10^6\ M^{-1}.s^{-1}$	[72]
$Gcamp_b$	GCaMP6s-Ca dissociation rate	1.12 s^{-1}	[72]
		IP_3R	
N_{IP_3R}	IP_3R number	50 molec.	[89]
d_{IP_3R}	IP_3R interact. distance	1 mesh triangle	-
		IP_3R binding	
a_1	First Ca	$1.2 \times 10^6\ M^{-1}.s^{-1}$	-
a_2	IP_3	$4.1 \times 10^7\ M^{-1}.s^{-1}$	-
a_3	Second Ca	$1.6 \times 10^4\ M^{-1}.s^{-1}$	-
		IP_3R dissociation	
b_1	First Ca	50 s^{-1}	-
b_2	IP_3	400 s^{-1}	-
b_3	Second Ca	100 s^{-1}	-

https://doi.org/10.1371/journal.pcbi.1006795.t002

Simulations code. The code of our ODE, Gillespie, Particle-based and STEPS models is available on ModelDB [133] at http://modeldb.yale.edu/247694.

Peak detection and analysis. Automated peak detection from model simulations was based on the statistics of baseline calcium trace. A histogram of Ca^{2+} trace was built with a bin size of 0.25 ions and the mode of this histogram was used to define baseline calcium. A peak initiation corresponded to the time step where calcium trace overcame a peak threshold defined as baseline + $n\sigma_{Ca}$ where σ_{Ca} is the standard deviation of the above histogram. The value of n varied between 2 and 4 and was set by hand for each simulation, depending on its signal/noise ratio. The peak was considered terminated when the calcium trace decreased again below peak threshold. This implies that in case of a second calcium peak starting before the first one terminated, both events were considered as being part of the same peak. Peak duration was defined as the full width at half maximum (FWHM). Peak amplitude was defined as the maximum number of

calcium ions reached during the peak duration. In the 3D model, the peak amplitude A was rescaled to facilitate comparison with experimental data, using $\Delta F/F = (A - C_{a_{baseline}})/C_{a_{baseline}}$, where $C_{a_{baseline}}$ is the basal calcium determined above. The number of IP_3R open per peak was defined as the maximum number of IP_3R open simultaneously during peak duration. Puffs were defined as calcium events resulting from the cooperation of more than one IP_3R. In our spatially-explicit simulations, a calcium signal was considered to be a puff if more than one IP_3R were open during the peak and if the average distance traveled by calcium within the duration of this peak was larger than the distance between the simultaneously open IP_3R molecules.

Experimental methods

All experiments were performed as described in [69]. We give below the main outlines of the methods. All experimental procedures were in accordance with the European Union and CNRS UMR5297 institutional guidelines for the care and use of laboratory animals (Council directive 2010/63/EU).

Organotypic hippocampal slice cultures. Organotypic hippocampal slices (Gähwiler type) were dissected from 5–7-d-old wild-type mice and cultured 5–8 week in a roller drum at 35°C, as previously described [134].

Viral infection. AAV9-GFAP-GCaMP6s [70] was injected by brief pressure pulses (40ms; 15 psi) into the stratum radiatum of 2-3-week old slices from Thy1-YFP-H (JAX:003782) mice 4-6 weeks prior to the experiment.

Image acquisition. For Ca^{2+} imaging, we used a custom-built setup based on an inverted microscope body (Leica DMI6000), as previously described in [135]. We used a 1.3 NA glycerol immersion objective equipped with a correction collar to reduce spherical aberrations and thereby allow imaging deeper inside brain tissue [136]. The excitation light was provided by a pulsed diode laser (l = 485 nm, PicoQuant, Berlin, Germany). The fluorescence signal was confocally detected by an avalanche photodiode (APD; SPCM-AQRH-14-FC; PerkinElmer). The spatial resolution of the setup was around 175 nm (in x-y) and 450 nm (z). Confocal time-lapse imaging (12.5 x 25 μm, pixel size 100 nm) was performed at 2Hz for 2.5 min in artificial cerebrospinal fluid containing 125 mM NaCl, 2.5 mM KCl, 1.3 mM $MgCl_2$, 2 mM $CaCl_2$, 26 mM $NaHCO_3$, 1.25 mM NaH_2PO_4, 20 mM D-glucose, 1 mM Trolox; 300 mOsm; pH 7.4. Perfusion rate was 2 mL/min and the temperature 32°C. Calcium traces are available at https://figshare. com/articles/Astrocytic_calcium_traces_from_organotypic_hippocampal_slices/8951006.

Image analysis. Spontaneous calcium events were detected and analyzed automatically by ImageJ plugin LC_Pro [137] and then manually verified using Igor Pro (Wavemetrics) [33].

Statistical analysis

For stochastic models, we generated 20 simulations (with different random numbers) and quantified these simulations as mean ± standard deviation over those 20 simulations. One-way ANOVA was performed to investigate the effect of a given parameter on calcium dynamics. Comparison between two simulation conditions were performed with unpaired Student T test if values followed a Gaussian distribution. Otherwise, a Mann-Whitney test was performed. The same method was applied to compare simulation to experimental results. Significance is assigned by $*$ for $p \leq 0.05$, $**$ for $p \leq 0.01$, $***$ for $p \leq 0.001$.

Supporting information

S1 Fig. Effect of adding buffers to the 2D particle-based model. (A) Biochemical reactions and regulatory interactions modeled in the 2D particle-based model in which endogenous

buffers ('Buf') were added. Reactions are the same as the ones described in Fig 1, except that Buf particles were added. The binding rate and dissociation constant associated with the binding of Ca^{2+} to Buf correspond respectively to buf_f and buf_b. Different amounts of endogenous Ca^{2+} buffers were added to the model (500 or 2000), with the following diffusion coefficients: D_{buf} = 0.1 a.u and D_{Ca} = 0.8 a.u. Those simulations were compared to our reference model, which contains no Buf particles but in which D_{Ca} = 0.1 a.u, corresponding to an effective lower D_{Ca}. No significant difference between simulations with a number of Buf of 0, 500 or 2000 is observed regarding basal Ca^{2+} concentration (B), peak amplitude (C) or peak frequency (D). Note that we refer here to free Ca^{2+} peaks and not to Buf-Ca peaks. Simulating Ca^{2+} diffusion in our 2D model with a decreased effective coefficient of diffusion is thus equivalent to simulating endogenous buffers of slower diffusion with faster diffusion of free Ca^{2+}.
(PDF)

S2 Fig. Reaction scheme of the 3D "GC+Buf" model. This figure presents the biochemical reactions and regulatory interactions modeled in the endogenous buffers model, "GC+Buf", in 3D. Reactions are the same as the ones described in Fig 1, except that new particles have been added: slow (CBs) and fast calbindin (CBf) as well as parvalbumin (PV), that can bind Ca^{2+} ions and diffuse, whether bound or not. Parameter values associated with this model are presented in S1 Table.
(PDF)

S1 Table. Parameter values and initial conditions associated to endogenous buffers in the 3D "GC+Buf" model. Parameter values for the "GC+Buf" 3d model described in supplemental S2 Fig are the same as in "GCaMP" model, presented in Table 2. Parameter values associated with endogenous kinetics and diffusion were taken from a study that modeled calcium dynamics in dendrites [127]. Note that total endogenous buffer concentration in our model is 2 orders of magnitude lower than in this study.
(PDF)

Acknowledgments

Author Contributions

Conceptualization: Audrey Denizot, Hédi Soula, Hugues Berry.

Data curation: Audrey Denizot, Misa Arizono, U. Valentin Nägerl.

Formal analysis: Audrey Denizot, Hédi Soula, Hugues Berry.

Funding acquisition: Hédi Soula, Hugues Berry.

Investigation: Audrey Denizot, Misa Arizono, U. Valentin Nägerl, Hédi Soula, Hugues Berry.

Methodology: Audrey Denizot, Hédi Soula, Hugues Berry.

Project administration: Hédi Soula, Hugues Berry.

Resources: Misa Arizono, U. Valentin Nägerl.

Software: Audrey Denizot, Hédi Soula, Hugues Berry.

Supervision: U. Valentin Nägerl, Hédi Soula, Hugues Berry.

Validation: Audrey Denizot, U. Valentin Nägerl, Hugues Berry.

Visualization: Audrey Denizot, Misa Arizono, Hédi Soula, Hugues Berry.

Writing – original draft: Audrey Denizot, Hédi Soula, Hugues Berry.

Writing – review & editing: Audrey Denizot, Misa Arizono, U. Valentin Nägerl, Hédi Soula, Hugues Berry.

References

1. Sontheimer H. Voltage-dependent ion channels in glial cells. Glia. 1994; 11(2):156–172. https://doi.org/10.1002/glia.440110210 PMID: 7523291

2. Orkand RK, Nicholls JG, Kuffler SW. Effect of nerve impulses on the membrane potential of glial cells in the central nervous system of amphibia. Journal of Neurophysiology. 1966; 29(4):788–806. https://doi.org/10.1152/jn.1966.29.4.788 PMID: 5966435

3. Cornell-Bell A, Finkbeiner S, Cooper M, Smith S. Glutamate induces calcium waves in cultured astrocytes: long-range glial signaling. Science. 1990; 247(4941):470–473.

4. Di Castro MA, Chuquet J, Liaudet N, Bhaukaurally K, Santello M, Bouvier D, et al. Local Ca2+ detection and modulation of synaptic release by astrocytes. Nature Neuroscience. 2011; 14(10):1276–1284. https://doi.org/10.1038/nn.2929 PMID: 21909085

5. Gómez-Gonzalo M, Navarrete M, Perea G, Covelo A, Martín-Fernández M, Shigemoto R, et al. Endocannabinoids Induce Lateral Long-Term Potentiation of Transmitter Release by Stimulation of Gliotransmission. Cerebral Cortex (New York, NY: 1991). 2015; 25(10):3699–3712.

6. Panatier A, Theodosis DT, Mothet JP, Touquet B, Pollegioni L, Poulain DA, et al. Glia-Derived d-Serine Controls NMDA Receptor Activity and Synaptic Memory. Cell. 2006; 125(4):775–784. https://doi.org/10.1016/j.cell.2006.02.051 PMID: 16713567

7. Takata N, Mishima T, Hisatsune C, Nagai T, Ebisui E, Mikoshiba K, et al. Astrocyte calcium signaling transforms cholinergic modulation to cortical plasticity in vivo. The Journal of Neuroscience: The Official Journal of the Society for Neuroscience. 2011; 31(49):18155–18165. https://doi.org/10.1523/JNEUROSCI.5289-11.2011

8. Metea MR, Newman EA. Glial Cells Dilate and Constrict Blood Vessels: A Mechanism of Neurovascular Coupling. Journal of Neuroscience. 2006; 26(11):2862–2870. https://doi.org/10.1523/JNEUROSCI.4048-05.2006 PMID: 16540563

9. Mulligan S, MacVicar B.A Mulligan S.J. & MacVicar B.A. Calcium transients in astrocyte endfeet cause cerebrovascular constrictions. Nature 431, 195-199. Nature. 2004; 431:195–9. https://doi.org/10.1038/nature02827 PMID: 15356633

10. Takano T, Tian GF, Peng W, Lou N, Libionka W, Han X, et al. Astrocyte-mediated control of cerebral blood flow. Nature Neuroscience. 2006; 9(2):260–267. https://doi.org/10.1038/nn1623 PMID: 16388306

11. Zonta M, Sebelin A, Gobbo S, Fellin T, Pozzan T, Carmignoto G. Glutamate-mediated cytosolic calcium oscillations regulate a pulsatile prostaglandin release from cultured rat astrocytes. The Journal of Physiology. 2003; 553(Pt 2):407–414. https://doi.org/10.1113/jphysiol.2003.046706 PMID: 14500777

12. Bazargani N, Attwell D. Astrocyte calcium signaling: the third wave. Nature Neuroscience. 2016; 19(2):182–189. https://doi.org/10.1038/nn.4201 PMID: 26814587

13. Perea G, Navarrete M, Araque A. Tripartite synapses: astrocytes process and control synaptic information. Trends in Neurosciences. 2009; 32(8):421–431. https://doi.org/10.1016/j.tins.2009.05.001 PMID: 19615761

14. Fiacco TA, McCarthy KD. Multiple Lines of Evidence Indicate That Gliotransmission Does Not Occur under Physiological Conditions. Journal of Neuroscience. 2018; 38(1):3–13. https://doi.org/10.1523/JNEUROSCI.0016-17.2017 PMID: 29298904

15. Savtchouk I, Volterra A. Gliotransmission: Beyond Black-and-White. Journal of Neuroscience. 2018; 38(1):14–25. https://doi.org/10.1523/JNEUROSCI.0017-17.2017 PMID: 29298905

16. Fellin T, Pascual O, Gobbo S, Pozzan T, Haydon PG, Carmignoto G. Neuronal Synchrony Mediated by Astrocytic Glutamate through Activation of Extrasynaptic NMDA Receptors. Neuron. 2004; 43(5):729–743. https://doi.org/10.1016/j.neuron.2004.08.011 PMID: 15339653

17. Perea G, Araque A. Properties of synaptically evoked astrocyte calcium signal reveal synaptic information processing by astrocytes. The Journal of Neuroscience: The Official Journal of the Society for Neuroscience. 2005; 25(9):2192–2203. https://doi.org/10.1523/JNEUROSCI.3965-04.2005

18. Morquette P, Verdier D, Kadala A, Féthière J, Philippe AG, Robitaille R, et al. An astrocyte-dependent mechanism for neuronal rhythmogenesis. Nature Neuroscience. 2015; 18(6):844–854. https://doi.org/10.1038/nn.4013 PMID: 25938883

19. Wang X, Lou N, Xu Q, Tian GF, Peng WG, Han X, et al. Astrocytic Ca2+ signaling evoked by sensory stimulation in vivo. Nature Neuroscience. 2006; 9(6):816–823. https://doi.org/10.1038/nn1703 PMID: 16699507

20. Asada A, Ujita S, Nakayama R, Oba S, Ishii S, Matsuki N, et al. Subtle modulation of ongoing calcium dynamics in astrocytic microdomains by sensory inputs. Physiological Reports. 2015; 3(10). https://doi.org/10.14814/phy2.12454 PMID: 26438730

21. Haustein MD, Kracun S, Lu XH, Shih T, Jackson-Weaver O, Tong X, et al. Conditions and constraints for astrocyte calcium signaling in the hippocampal mossy fiber pathway. Neuron. 2014; 82(2):413–429. https://doi.org/10.1016/j.neuron.2014.02.041 PMID: 24742463

22. Morita M, Higuchi C, Moto T, Kozuka N, Susuki J, Itofusa R, et al. Dual Regulation of Calcium Oscillation in Astrocytes by Growth Factors and Pro-Inflammatory Cytokines via the Mitogen-Activated Protein Kinase Cascade. Journal of Neuroscience. 2003; 23(34):10944–10952. https://doi.org/10.1523/JNEUROSCI.23-34-10944.2003 PMID: 14645490

23. Nett WJ, Oloff SH, McCarthy KD. Hippocampal Astrocytes In Situ Exhibit Calcium Oscillations That Occur Independent of Neuronal Activity. Journal of Neurophysiology. 2002; 87(1):528–537. https://doi.org/10.1152/jn.00268.2001 PMID: 11784768

24. Parri HR, Crunelli V. The role of Ca2+ in the generation of spontaneous astrocytic Ca2+ oscillations. Neuroscience. 2003; 120(4):979–992. https://doi.org/10.1016/s0306-4522(03)00379-8 PMID: 12927204

25. Zur Nieden R, Deitmer JW. The role of metabotropic glutamate receptors for the generation of calcium oscillations in rat hippocampal astrocytes in situ. Cerebral Cortex (New York, NY: 1991). 2006; 16 (5):676–687.

26. Panatier A, Vallée J, Haber M, Murai KK, Lacaille JC, Robitaille R. Astrocytes are endogenous regulators of basal transmission at central synapses. Cell. 2011; 146(5):785–798. https://doi.org/10.1016/j.cell.2011.07.022 PMID: 21855979

27. Grosche J, Matyash V, Möller T, Verkhratsky A, Reichenbach A, Kettenmann H. Microdomains for neuron?glia interaction: parallel fiber signaling to Bergmann glial cells. Nature Neuroscience. 1999; 2 (2):139–143. https://doi.org/10.1038/5692 PMID: 10195197

28. Srinivasan R, Huang BS, Venugopal S, Johnston AD, Chai H, Zeng H, et al. Ca(2+) signaling in astrocytes from Ip3r2(-/-) mice in brain slices and during startle responses in vivo. Nature Neuroscience. 2015; 18(5):708–717. https://doi.org/10.1038/nn.4001 PMID: 25894291

29. Beierlein M, Regehr WG. Brief Bursts of Parallel Fiber Activity Trigger Calcium Signals in Bergmann Glia. Journal of Neuroscience. 2006; 26(26):6958–6967. https://doi.org/10.1523/JNEUROSCI.0613-06.2006 PMID: 16807325

30. Matyash V, Filippov V, Mohrhagen K, Kettenmann H. Nitric Oxide Signals Parallel Fiber Activity to Bergmann Glial Cells in the Mouse Cerebellar Slice. Molecular and Cellular Neuroscience. 2001; 18 (6):664–670. https://doi.org/10.1006/mcne.2001.1047 PMID: 11749041

31. Newman EA. Propagation of Intercellular Calcium Waves in Retinal Astrocytes and Müller Cells. Journal of Neuroscience. 2001; 21(7):2215–2223. https://doi.org/10.1523/JNEUROSCI.21-07-02215.2001 PMID: 11264297

32. Cahoy JD, Emery B, Kaushal A, Foo LC, Zamanian JL, Christopherson KS, et al. A Transcriptome Database for Astrocytes, Neurons, and Oligodendrocytes: A New Resource for Understanding Brain Development and Function. Journal of Neuroscience. 2008; 28(1):264–278. https://doi.org/10.1523/JNEUROSCI.4178-07.2008 PMID: 18171944

33. Sherwood MW, Arizono M, Hisatsune C, Bannai H, Ebisui E, Sherwood JL, et al. Astrocytic IP3Rs: Contribution to Ca2+ signalling and hippocampal LTP. Glia. 2017; 65(3):502–513. https://doi.org/10.1002/glia.23107 PMID: 28063222

34. Fiacco TA, Agulhon C, McCarthy KD. Sorting Out Astrocyte Physiology from Pharmacology. Annual Review of Pharmacology and Toxicology. 2009; 49(1):151–174. https://doi.org/10.1146/annurev.pharmtox.011008.145602 PMID: 18834310

35. Porter JT, McCarthy KD. Astrocytic neurotransmitter receptors in situ and in vivo. Progress in Neurobiology. 1997; 51(4):439–455. https://doi.org/10.1016/S0301-0082(96)00068-8 PMID: 9106901

36. Bosanac I, Alattia JR, Mal TK, Chan J, Talarico S, Tong FK, et al. Structure of the inositol 1,4,5-trisphosphate receptor binding core in complex with its ligand. Nature. 2002; 420(6916):696–700. https://doi.org/10.1038/nature01268 PMID: 12442173

37. Panatier A, Arizono M, Nägerl UV. Dissecting tripartite synapses with STED microscopy. Phil Trans R Soc B. 2014; 369(1654):20130597. https://doi.org/10.1098/rstb.2013.0597 PMID: 25225091

38. Bindocci E, Savtchouk I, Liaudet N, Becker D, Carriero G, Volterra A. Three-dimensional Ca^{2+} imaging advances understanding of astrocyte biology. Science. 2017; 356(6339):eaai8185. https://doi.org/10.1126/science.aai8185 PMID: 28522470

39. Ventura R, Harris KM. Three-Dimensional Relationships between Hippocampal Synapses and Astrocytes. The Journal of Neuroscience. 1999; 19(16):6897–6906. https://doi.org/10.1523/JNEUROSCI.19-16-06897.1999 PMID: 10436047

40. Rusakov DA. Disentangling calcium-driven astrocyte physiology. Nature Reviews Neuroscience. 2015; 16(4):226–233. https://doi.org/10.1038/nrn3878 PMID: 25757560

41. Thillaiappan NB, Chavda A, Tovey S, Prole D, Taylor C. Ca2+ signals initiate at immobile IP3 receptors adjacent to ER-plasma membrane junctions. Nature Communications. 2017; 8. https://doi.org/10.1038/s41467-017-01644-8 PMID: 29138405

42. Smith IF, Wiltgen SM, Parker I. Localization of puff sites adjacent to the plasma membrane: Functional and spatial characterization of Ca2+ signaling in SH-SY5Y cells utilizing membrane-permeant caged IP3. Cell Calcium. 2009; 45(1):65–76. https://doi.org/10.1016/j.ceca.2008.06.001 PMID: 18639334

43. Manninen T, Havela R, Linne ML. Reproducibility and Comparability of Computational Models for Astrocyte Calcium Excitability. Frontiers in Neuroinformatics. 2017; 11. https://doi.org/10.3389/fninf.2017.00011 PMID: 28270761

44. Oschmann F, Berry H, Obermayer K, Lenk K. From in silico astrocyte cell models to neuron-astrocyte network models: A review. Brain Research Bulletin. 2017. https://doi.org/10.1016/j.brainresbull.2017.01.027 PMID: 28189516

45. Manninen T, Havela R, Linne ML. Computational Models for Calcium-Mediated Astrocyte Functions. Frontiers in Computational Neuroscience. 2018; 12. https://doi.org/10.3389/fncom.2018.00014 PMID: 29670517

46. De Young GW, Keizer J. A single-pool inositol 1,4,5-trisphosphate-receptor-based model for agonist-stimulated oscillations in Ca2+ concentration. Proceedings of the National Academy of Sciences. 1992; 89(20):9895–9899. https://doi.org/10.1073/pnas.89.20.9895

47. Goldbetter A, Dupont G, Berridge MJ. Minimal Model for Signal-Induced Ca2+ Oscillations and for Their Frequency Encoding Through Protein Phosphorylation. Proceedings of the National Academy of Science. 1990; 87:1461–1465. https://doi.org/10.1073/pnas.87.4.1461

48. Li YX, Rinzel J. Equations for InsP3 Receptor-mediated [Ca2+]i Oscillations Derived from a Detailed Kinetic Model: A Hodgkin-Huxley Like Formalism. Journal of Theoretical Biology. 1994; 166(4):461–473. https://doi.org/10.1006/jtbi.1994.1041 PMID: 8176949

49. Pittà MD, Goldberg M, Volman V, Berry H, Ben-Jacob E. Glutamate regulation of calcium and IP<Subscript>3</Subscript> oscillating and pulsating dynamics in astrocytes. Journal of Biological Physics. 2009; 35(4):383–411. https://doi.org/10.1007/s10867-009-9155-y

50. Goto I, Kinoshita S, Natsume K. The model of glutamate-induced intracellular Ca2+ oscillation and intercellular Ca2+ wave in brain astrocytes. Neurocomputing—IJON. 2004; 58:461–467.

51. Falcke M, Tsimring L, Levine H. Stochastic spreading of intracellular Ca(2+) release. Physical Review E, Statistical Physics, Plasmas, Fluids, and Related Interdisciplinary Topics. 2000; 62(2 Pt B):2636–2643. PMID: 11088743

52. Rüdiger S, Shuai JW, Huisinga W, Nagaiah C, Warnecke G, Parker I, et al. Hybrid stochastic and deterministic simulations of calcium blips. Biophysical Journal. 2007; 93(6):1847–1857. https://doi.org/10.1529/biophysj.106.099879 PMID: 17496042

53. Rüdiger S, Nagaiah C, Warnecke G, Shuai JW. Calcium Domains around Single and Clustered IP3 Receptors and Their Modulation by Buffers. Biophysical Journal. 2010; 99(1):3–12. https://doi.org/10.1016/j.bpj.2010.02.059 PMID: 20655827

54. Skupin A, Kettenmann H, Falcke M. Calcium Signals Driven by Single Channel Noise. PLoS computational biology. 2010; 6. https://doi.org/10.1371/journal.pcbi.1000870 PMID: 20700497

55. Dobramysl U, Rüdiger S, Erban R. Particle-Based Multiscale Modeling of Calcium Puff Dynamics. Multiscale Modeling & Simulation. 2016; p. 997–1016. https://doi.org/10.1137/15M1015030

56. Bezprozvanny I, Watras J, Ehrlich BE. Bell-shaped calcium-response curves of Ins(1,4,5)P3- and calcium-gated channels from endoplasmic reticulum of cerebellum. Nature. 1991; 351(6329):751–754. https://doi.org/10.1038/351751a0 PMID: 1648178

57. Swillens S, Dupont G, Combettes L, Champeil P. From calcium blips to calcium puffs: theoretical analysis of the requirements for interchannel communication. Proceedings of the National Academy of

Sciences of the United States of America. 1999; 96(24):13750–13755. https://doi.org/10.1073/pnas.96.24.13750 PMID: 10570144

58. Smith IF, Wiltgen SM, Shuai J, Parker I. Ca2+ Puffs Originate from Preestablished Stable Clusters of Inositol Trisphosphate Receptors. Sci Signal. 2009; 2(98):ra77–ra77. https://doi.org/10.1126/scisignal.2000466 PMID: 19934435

59. Dickinson G, Swaminathan D, Parker I. The Probability of Triggering Calcium Puffs Is Linearly Related to the Number of Inositol Trisphosphate Receptors in a Cluster. Biophysical Journal. 2012; 102 (8):1826–1836. https://doi.org/10.1016/j.bpj.2012.03.029 PMID: 22768938

60. Flegg MB, Rüdiger S, Erban R. Diffusive spatio-temporal noise in a first-passage time model for intracellular calcium release. The Journal of Chemical Physics. 2013; 138(15):154103. https://doi.org/10.1063/1.4796417 PMID: 23614408

61. Pando B, Dawson SP, Mak DOD, Pearson JE. Messages diffuse faster than messengers. Proceedings of the National Academy of Sciences. 2006; 103(14):5338–5342. https://doi.org/10.1073/pnas.0509576103

62. Fraiman D, Dawson SP. Buffer regulation of calcium puff sequences. Physical Biology. 2014; 11 (1):016007. https://doi.org/10.1088/1478-3975/11/1/016007 PMID: 24476691

63. Falcke M. Buffers and oscillations in intracellular Ca2+ dynamics. Biophysical Journal. 2003; 84 (1):28–41. https://doi.org/10.1016/S0006-3495(03)74830-9 PMID: 12524263

64. Shuai J, Pearson JE, Parker I. Modeling Ca2+ Feedback on a Single Inositol 1,4,5-Trisphosphate Receptor and Its Modulation by Ca2+ Buffers. Biophysical Journal. 2008; 95(8):3738–3752. https://doi.org/10.1529/biophysj.108.137182 PMID: 18641077

65. Lencesova L, O'Neill A, Resneck WG, Bloch RJ, Blaustein MP. Plasma membrane-cytoskeleton-endoplasmic reticulum complexes in neurons and astrocytes. The Journal of Biological Chemistry. 2004; 279(4):2885–2893. https://doi.org/10.1074/jbc.M310365200 PMID: 14593108

66. Weerth SH, Holtzclaw LA, Russell JT. Signaling proteins in raft-like microdomains are essential for Ca2+ wave propagation in glial cells. Cell Calcium. 2007; 41(2):155–167. https://doi.org/10.1016/j.ceca.2006.06.006 PMID: 16905188

67. Buscemi L, Ginet V, Lopatar J, Montana V, Pucci L, Spagnuolo P, et al. Homer1 Scaffold Proteins Govern Ca2+ Dynamics in Normal and Reactive Astrocytes. Cerebral Cortex (New York, NY: 1991). 2016.

68. Xiao B, Tu JC, Worley PF. Homer: a link between neural activity and glutamate receptor function. Current Opinion in Neurobiology. 2000; 10(3):370–374. https://doi.org/10.1016/S0959-4388(00)00087-8 PMID: 10851183

69. Arizono M, Panatier A, Inavalli VVGK, Pfeiffer T, Angibaud J, Stobart J, et al. Structural Basis of Astrocytic Ca^2 Signals at Tripartite Synapses. Rochester, NY: Social Science Research Network; 2018. ID 3287791. Available from: https://papers.ssrn.com/abstract=3287791.

70. Stobart JL, Ferrari KD, Barrett MJP, Stobart MJ, Looser ZJ, Saab AS, et al. Long-term In Vivo Calcium Imaging of Astrocytes Reveals Distinct Cellular Compartment Responses to Sensory Stimulation. Cerebral Cortex (New York, NY: 1991). 2018; 28(1):184–198.

71. Skupin A, Kettenmann H, Winkler U, Wartenberg M, Sauer H, Tovey SC, et al. How Does Intracellular Ca2+ Oscillate: By Chance or by the Clock? Biophysical Journal. 2008; 94(6):2404–2411. https://doi.org/10.1529/biophysj.107.119495 PMID: 18065468

72. Chen TW, Wardill TJ, Sun Y, Pulver SR, Renninger SL, Baohan A, et al. Ultrasensitive fluorescent proteins for imaging neuronal activity. Nature. 2013; 499(7458):295–300. https://doi.org/10.1038/nature12354 PMID: 23868258

73. Patrushev I, Gavrilov N, Turlapov V, Semyanov A. Subcellular location of astrocytic calcium stores favors extrasynaptic neuron-astrocyte communication. Cell Calcium. 2013; 54(5):343–349. https://doi.org/10.1016/j.ceca.2013.08.003 PMID: 24035346

74. Montes de Oca Balderas P, Montes de Oca Balderas H. Synaptic neuron-astrocyte communication is supported by an order of magnitude analysis of inositol tris-phosphate diffusion at the nanoscale in a model of peri-synaptic astrocyte projection. BMC Biophysics. 2018; 11:3. https://doi.org/10.1186/s13628-018-0043-3 PMID: 29456837

75. Boulay AC, Saubaméa B, Adam N, Chasseigneaux S, Mazaré N, Gilbert A, et al. Translation in astrocyte distal processes sets molecular heterogeneity at the gliovascular interface. Cell Discovery. 2017; 3:17005. https://doi.org/10.1038/celldisc.2017.5 PMID: 28377822

76. Jones VC, McKeown L, Verkhratsky A, Jones OT. LV-pIN-KDEL: a novel lentiviral vector demonstrates the morphology, dynamics and continuity of the endoplasmic reticulum in live neurones. BMC Neuroscience. 2008; 9:10. https://doi.org/10.1186/1471-2202-9-10 PMID: 18215281

77. Nixon-Abell J, Obara CJ, Weigel AV, Li D, Legant WR, Xu CS, et al. Increased spatiotemporal resolution reveals highly dynamic dense tubular matrices in the peripheral ER. Science. 2016; 354(6311): aaf3928. https://doi.org/10.1126/science.aaf3928 PMID: 27789813

78. Brunstein M, Wicker K, Hérault K, Heintzmann R, Oheim M. Full-field dual-color 100-nm super-resolution imaging reveals organization and dynamics of mitochondrial and ER networks. Optics Express. 2013; 21(22):26162–26173. https://doi.org/10.1364/OE.21.026162 PMID: 24216840

79. Kopek BG, Paez-Segala MG, Shtengel G, Sochacki KA, Sun MG, Wang Y, et al. Diverse protocols for correlative super-resolution fluorescence imaging and electron microscopy of chemically fixed samples. Nature protocols. 2017; 12(5):916–946. https://doi.org/10.1038/nprot.2017.017 PMID: 28384138

80. Okubo Y, Kanemaru K, Suzuki J, Kobayashi K, Hirose K, Iino M. Inositol 1,4,5-trisphosphate receptor type 2-independent Ca2+ release from the endoplasmic reticulum in astrocytes. Glia. 2019; 67 (1):113–124. https://doi.org/10.1002/glia.23531 PMID: 30306640

81. Bannai H, Hirose M, Niwa F, Mikoshiba K. Dissection of Local Ca2+ Signals in Cultured Cells by Membrane targeted Ca2+ Indicators. JoVE (Journal of Visualized Experiments). 2019;(145):e59246.

82. Alzayady KJ, Sebé-Pedrós A, Chandrasekhar R, Wang L, Ruiz-Trillo I, Yule DI. Tracing the Evolutionary History of Inositol, 1, 4, 5-Trisphosphate Receptor: Insights from Analyses of Capsaspora owczarzaki Ca2+ Release Channel Orthologs. Molecular Biology and Evolution. 2015; 32(9):2236–2253. https://doi.org/10.1093/molbev/msv098 PMID: 25911230

83. Serysheva II, Baker MR, Fan G. Structural Insights into IP₃R Function. In: Membrane Dynamics and Calcium Signaling. Advances in Experimental Medicine and Biology. Springer, Cham; 2017. p. 121–147. Available from: https://link.springer.com/chapter/10.1007/978-3-319-55858-5_6.

84. Bicknell BA, Goodhill GJ. Emergence of ion channel modal gating from independent subunit kinetics. Proceedings of the National Academy of Sciences. 2016; 113(36):E5288–E5297. https://doi.org/10.1073/pnas.1604090113

85. Oura T, Murata K, Morita T, Nezu A, Arisawa M, Shuto S, et al. Highly Sensitive Measurement of Inositol 1,4,5-Trisphosphate by Using a New Fluorescent Ligand and Ligand Binding Domain Combination. Chembiochem: A European Journal of Chemical Biology. 2016; 17(16):1509–1512. https://doi.org/10.1002/cbic.201600096 PMID: 27251449

86. Zheng K, Bard L, Reynolds JP, King C, Jensen T, Gourine A, et al. Time-Resolved Imaging Reveals Heterogeneous Landscapes of Nanomolar Ca2+ in Neurons and Astroglia. Neuron. 2015; 88(2):277–288. https://doi.org/10.1016/j.neuron.2015.09.043 PMID: 26494277

87. Gin E, Falcke M, Wagner LE, Yule DI, Sneyd J. A Kinetic Model of the Inositol Trisphosphate Receptor Based on Single-Channel Data. Biophysical Journal. 2009; 96(10):4053–4062. https://doi.org/10.1016/j.bpj.2008.12.3964 PMID: 19450477

88. Siekmann I, Wagner L, Yule D, Crampin E, Sneyd J. A Kinetic Model for Type I and II IP3R Accounting for Mode Changes. Biophysical Journal. 2012; 103(4):658–668. https://doi.org/10.1016/j.bpj.2012.07.016 PMID: 22947927

89. Wiltgen SM, Smith IF, Parker I. Superresolution localization of single functional IP3R channels utilizing Ca2+ flux as a readout. Biophysical Journal. 2010; 99(2):437–446. PMID: 20643061

90. Tay LH, Dick IE, Yang W, Mank M, Griesbeck O, Yue DT. Nanodomain Ca^{2+} of Ca^{2+} channels detected by a tethered genetically encoded Ca^{2+} sensor. Nature Communications. 2012; 3:778. https://doi.org/10.1038/ncomms1777 PMID: 22491326

91. Tadross MR, Tsien RW, Yue DT. Ca2+ channel nanodomains boost local Ca2+ amplitude. Proceedings of the National Academy of Sciences of the United States of America. 2013; 110(39):15794–15799. https://doi.org/10.1073/pnas.1313898110 PMID: 24019485

92. Sun MY, Devaraju P, Xie AX, Holman I, Samones E, Murphy TR, et al. Astrocyte calcium microdomains are inhibited by Bafilomycin A1 and cannot be replicated by low-level Schaffer collateral stimulation in situ. Cell Calcium. 2014; 55(1):1–16. https://doi.org/10.1016/j.ceca.2013.10.004 PMID: 24262208

93. Agarwal A, Wu PH, Hughes EG, Fukaya M, Tischfield MA, Langseth AJ, et al. Transient Opening of the Mitochondrial Permeability Transition Pore Induces Microdomain Calcium Transients in Astrocyte Processes. Neuron. 2017; 93(3):587–605.e7. https://doi.org/10.1016/j.neuron.2016.12.034 PMID: 28132831

94. Mauvezin C, Neufeld TP. Bafilomycin A1 disrupts autophagic flux by inhibiting both V-ATPase-dependent acidification and Ca-P60A/SERCA-dependent autophagosome-lysosome fusion. Autophagy. 2015; 11(8):1437–1438. https://doi.org/10.1080/15548627.2015.1066957 PMID: 26156798

95. Roest G, La Rovere RM, Bultynck G, Parys JB. IP3 Receptor Properties and Function at Membrane Contact Sites. Advances in Experimental Medicine and Biology. 2017; 981:149–178. https://doi.org/10.1007/978-3-319-55858-5_7 PMID: 29594861

96. Wilson BS, Pfeiffer JR, Smith AJ, Oliver JM, Oberdorf JA, Wojcikiewicz RJH. Calcium-dependent Clustering of Inositol 1,4,5-Trisphosphate Receptors. Molecular Biology of the Cell. 1998; 9(6):1465–1478. https://doi.org/10.1091/mbc.9.6.1465 PMID: 9614187

97. Rahman T. Dynamic clustering of IP$_3$ receptors by IP3. Biochemical Society Transactions. 2012; 40 (2):325–330. https://doi.org/10.1042/BST20110772 PMID: 22435806

98. Smith I, Swaminathan D, Dickinson G, Parker I. Single-Molecule Tracking of Inositol Trisphosphate Receptors Reveals Different Motilities and Distributions. Biophysical Journal. 2014; 107(4):834–845. https://doi.org/10.1016/j.bpj.2014.05.051 PMID: 25140418

99. Shuai JW, Jung P. Optimal ion channel clustering for intracellular calcium signaling. Proceedings of the National Academy of Sciences. 2003; 100(2):506–510. https://doi.org/10.1073/pnas.0236032100

100. Skupin A, Falcke M. The role of IP3R clustering in Ca2+ signaling. Genome Informatics International Conference on Genome Informatics. 2008; 20:15–24. PMID: 19425119

101. Means S, Smith AJ, Shepherd J, Shadid J, Fowler J, Wojcikiewicz RJH, et al. Reaction Diffusion Modeling of Calcium Dynamics with Realistic ER Geometry. Biophysical Journal. 2006; 91(2):537–557. https://doi.org/10.1529/biophysj.105.075036 PMID: 16617072

102. Tu H, Wang Z, Bezprozvanny I. Modulation of Mammalian Inositol 1,4,5-Trisphosphate Receptor Isoforms by Calcium: A Role of Calcium Sensor Region. Biophysical Journal. 2005; 88(2):1056–1069. https://doi.org/10.1529/biophysj.104.049601 PMID: 15531634

103. Tu H, Wang Z, Nosyreva E, De Smedt H, Bezprozvanny I. Functional Characterization of Mammalian Inositol 1,4,5-Trisphosphate Receptor Isoforms. Biophysical Journal. 2005; 88(2):1046–1055. https://doi.org/10.1529/biophysj.104.049593 PMID: 15533917

104. Taylor CW. Regulation of IP3 receptors by cyclic AMP. Cell Calcium. 2017; 63:48–52. https://doi.org/10.1016/j.ceca.2016.10.005 PMID: 27836216

105. Thrower EC, Hagar RE, Ehrlich BE. Regulation of Ins(1,4,5)P3 receptor isoforms by endogenous modulators. Trends in Pharmacological Sciences. 2001; 22(11):580–586. https://doi.org/10.1016/S0165-6147(00)01809-5 PMID: 11698102

106. Wagner LE, Yule DI. Differential regulation of the InsP? receptor type-1 and -2 single channel properties by InsP3, Ca2+ and ATP. The Journal of Physiology. 2012; 590(14):3245–3259. https://doi.org/10.1113/jphysiol.2012.228320 PMID: 22547632

107. Allbritton NL, Meyer T, Stryer L. Range of messenger action of calcium ion and inositol 1,4,5-trisphosphate. Science (New York, NY). 1992; 258(5089):1812–1815. https://doi.org/10.1126/science.1465619

108. Wang Z, Tymianski M, Jones OT, Nedergaard M. Impact of Cytoplasmic Calcium Buffering on the Spatial and Temporal Characteristics of Intercellular Calcium Signals in Astrocytes. Journal of Neuroscience. 1997; 17(19):7359–7371. https://doi.org/10.1523/JNEUROSCI.17-19-07359.1997 PMID: 9295382

109. Zeller S, Rüdiger S, Engel H, Sneyd J, Warnecke G, Parker I, et al. Modeling of the modulation by buffers of Ca2+ release through clusters of IP3 receptors. Biophysical Journal. 2009; 97(4):992–1002. https://doi.org/10.1016/j.bpj.2009.05.050 PMID: 19686646

110. Wieder N, Fink R, von Wegner F. Exact Stochastic Simulation of a Calcium Microdomain Reveals the Impact of Ca2+ Fluctuations on IP3R Gating. Biophysical Journal. 2015; 108(3):557–567. https://doi.org/10.1016/j.bpj.2014.11.3458 PMID: 25650923

111. Schwaller B. Cytosolic Ca2+ buffers. Cold Spring Harbor Perspectives in Biology. 2010; 2(11): a004051. https://doi.org/10.1101/cshperspect.a004051 PMID: 20943758

112. Chai H, Diaz-Castro B, Shigetomi E, Monte E, Octeau JC, Yu X, et al. Neural Circuit-Specialized Astrocytes: Transcriptomic, Proteomic, Morphological, and Functional Evidence. Neuron. 2017; 95(3):531–549.e9. https://doi.org/10.1016/j.neuron.2017.06.029 PMID: 28712653

113. Haim LB, Rowitch DH. Functional diversity of astrocytes in neural circuit regulation. Nature Reviews Neuroscience. 2017; 18(1):31–41. https://doi.org/10.1038/nrn.2016.159 PMID: 27904142

114. Breslin K, Wade JJ, Wong-Lin K, Harkin J, Flanagan B, Zalinge HV, et al. Potassium and sodium microdomains in thin astroglial processes: A computational model study. PLOS Computational Biology. 2018; 14(5):e1006151. https://doi.org/10.1371/journal.pcbi.1006151 PMID: 29775457

115. Khalid MU, Tervonen A, Korkka I, Hyttinen J, Lenk K. Geometry-based Computational Modeling of Calcium Signaling in an Astrocyte. In: EMBEC & NBC 2017. IFMBE Proceedings. Springer, Singapore; 2017. p. 157–160. Available from: https://link.springer.com/chapter/10.1007/978-981-10-5122-7_40.

116. Savtchenko LP, Bard L, Jensen TP, Reynolds JP, Kraev I, Medvedev N, et al. Disentangling astroglial physiology with a realistic cell model in silico. Nature Communications. 2018; 9(1):3554. https://doi.org/10.1038/s41467-018-05896-w PMID: 30177844

117. Gillespie DT. Exact stochastic simulation of coupled chemical reactions. The Journal of Physical Chemistry. 1977; 81(25):2340–2361. https://doi.org/10.1021/j100540a008

118. Gillespie DT. Stochastic simulation of chemical kinetics. Annual Review of Physical Chemistry. 2007; 58:35–55. https://doi.org/10.1146/annurev.physchem.58.032806.104637 PMID: 17037977

119. Isaacson SA, Isaacson D. The Reaction-Diffusion Master Equation, Diffusion Limited Reactions, and Singular Potentials. Physical Review E, Statistical, Nonlinear, and Soft Matter Physics. 2009; 80(6 Pt 2):066106. https://doi.org/10.1103/PhysRevE.80.066106 PMID: 20365230

120. Smith S, Grima R. Spatial Stochastic Intracellular Kinetics: A Review of Modelling Approaches. Bulletin of Mathematical Biology. 2018.

121. Hepburn I, Chen W, Wils S, De Schutter E. STEPS: efficient simulation of stochastic reaction?diffusion models in realistic morphologies. BMC Systems Biology. 2012; 6(1):36. https://doi.org/10.1186/1752-0509-6-36 PMID: 22574658

122. Wils S, De Schutter E. STEPS: Modeling and Simulating Complex Reaction-Diffusion Systems with Python. Frontiers in Neuroinformatics. 2009; 3:15. https://doi.org/10.3389/neuro.11.015.2009 PMID: 19623245

123. Chen W, De Schutter E. Parallel STEPS: Large Scale Stochastic Spatial Reaction-Diffusion Simulation with High Performance Computers. Frontiers in Neuroinformatics. 2017; 11. https://doi.org/10.3389/fninf.2017.00013 PMID: 28239346

124. Shigetomi E, Patel S, Khakh BS. Probing the Complexities of Astrocyte Calcium Signaling. Trends in Cell Biology. 2016; 26(4):300–312. https://doi.org/10.1016/j.tcb.2016.01.003 PMID: 26896246

125. Swaminathan D, Jung P. The Role of agonist-independent conformational transformation (AICT) in IP3 cluster behavior. Cell Calcium. 2011; 49(3):145–152. https://doi.org/10.1016/j.ceca.2010.11.003 PMID: 21334066

126. Hituri K, Linne ML. Comparison of Models for IP3 Receptor Kinetics Using Stochastic Simulations. PLOS ONE. 2013; 8(4):e59618. https://doi.org/10.1371/journal.pone.0059618 PMID: 23630568

127. Anwar H, Hepburn I, Nedelescu H, Chen W, Schutter ED. Stochastic Calcium Mechanisms Cause Dendritic Calcium Spike Variability. Journal of Neuroscience. 2013; 33(40):15848–15867. https://doi.org/10.1523/JNEUROSCI.1722-13.2013 PMID: 24089492

128. Calì C, Baghabra J, Boges DJ, Holst GR, Kreshuk A, Hamprecht FA, et al. Three-dimensional immersive virtual reality for studying cellular compartments in 3D models from EM preparations of neural tissues. Journal of Comparative Neurology. 2016; 524(1):23–38. https://doi.org/10.1002/cne.23852 PMID: 26179415

129. Hernàndez-Sotomayor SMT, Santos-Briones CDL, Muñoz-Sànchez JA, Loyola-Vargas VM. Kinetic Analysis of Phospholipase C from Catharanthus roseus Transformed Roots Using Different Assays. Plant Physiology. 1999; 120(4):1075–1082. https://doi.org/10.1104/pp.120.4.1075 PMID: 10444091

130. Akerboom J, Chen TW, Wardill TJ, Tian L, Marvin JS, Mutlu S, et al. Optimization of a GCaMP calcium indicator for neural activity imaging. The Journal of Neuroscience: The Official Journal of the Society for Neuroscience. 2012; 32(40):13819–13840. https://doi.org/10.1523/JNEUROSCI.2601-12.2012

131. Hires SA, Tian L, Looger LL. Reporting neural activity with genetically encoded calcium indicators. Brain Cell Biology. 2008; 36(1-4):69. https://doi.org/10.1007/s11068-008-9029-4 PMID: 18941901

132. Michailova A, Del Principe F, Egger M, Niggli E. Spatiotemporal Features of Ca2+ Buffering and Diffusion in Atrial Cardiac Myocytes with Inhibited Sarcoplasmic Reticulum. Biophysical journal. 2003; 83:3134–51. https://doi.org/10.1016/S0006-3495(02)75317-4

133. McDougal RA, Morse TM, Carnevale T, Marenco L, Wang R, Migliore M, et al. Twenty years of ModelDB and beyond: building essential modeling tools for the future of neuroscience. Journal of Computational Neuroscience. 2017; 42(1):1–10. https://doi.org/10.1007/s10827-016-0623-7 PMID: 27629590

134. Gähwiler BH. Organotypic monolayer cultures of nervous tissue. Journal of Neuroscience Methods. 1981; 4(4):329–342. https://doi.org/10.1016/0165-0270(81)90003-0 PMID: 7033675

135. Tønnesen J, Nadrigny F, Willig K, Wedlich-Söldner R, Nägerl UV. Two-Color STED Microscopy of Living Synapses Using A Single Laser-Beam Pair. Biophysical Journal. 2011; 101(10):2545–2552. https://doi.org/10.1016/j.bpj.2011.10.011 PMID: 22098754

136. Urban N, Willig K, Hell S, Nägerl UV. STED Nanoscopy of Actin Dynamics in Synapses Deep Inside Living Brain Slices. Biophysical Journal. 2011; 101(5):1277–1284. https://doi.org/10.1016/j.bpj.2011.07.027 PMID: 21889466

137. Francis M, Waldrup J, Qian X, Taylor MS. Automated Analysis of Dynamic Ca2+ Signals in Image Sequences. Journal of Visualized Experiments: JoVE. 2014;(88). https://doi.org/10.3791/51560